

An Online Ensemble Coupled Data Assimilation Capability for the Community Earth System Model: System Design and Evaluation

Jingzhe Sun^{★,5}, Yingjing Jiang^{★,1,4}, Shaoqing Zhang^{*1,3,4}, Weimin Zhang^{*2}, Lv Lu^{1,4}, Guangliang Liu⁶, Yuhu Chen³, Xiang Xing², Xiaopei Lin^{1,3,4} and Lixin Wu^{1,3,4}

5 ¹Key Laboratory of Physical Oceanography, Ministry of Education/Institute for Advanced Ocean Study/Frontiers Science Center for Deep Ocean Multispheres and Earth System (DOMES), Ocean University of China, Qingdao, China

²Southern Marine Science and Engineering Guangdong Laboratory, Zhuhai, China

³Qingdao Pilot National Laboratory for Marine Science and Technology (QNLN), Qingdao, China

⁴The College of Oceanic and Atmospheric Sciences, Ocean University of China, Qingdao, China

10 ⁵Beijing Institute of Applied Meteorology, Beijing, China

⁶Shandong Provincial Key Laboratory of Computer Networks, Qilu University of Technology (Shandong Academy of Sciences), Jinan, China

*Corresponding author: S. Zhang(szhang@ouc.edu.cn); W. Zhang (wmzhang104@139.com)

15 ★ These authors contributed equally to this work.

Abstract. The Community Earth System Model (CESM) developed at the National Center of Atmospheric Research (NCAR) has been used worldwide for climate studies. This study extends the efforts of CESM development to include an online (i.e., in-core) ensemble coupled data assimilation system (CESM-ECDA) to enhance CESM's capability for climate predictability 20 studies and prediction applications. The CESM-ECDA system consists of an online atmospheric data assimilation (ADA) component implemented to both the finite-volume and spectral-element dynamical cores, and an online oceanic data assimilation (ODA) component. In ADA, surface pressures (Ps) are assimilated, while in ODA, gridded sea surface temperature (SST) and ocean temperature and salinity profiles at real Argo locations are assimilated. The system has been evaluated within a perfect twin experiment framework, showing significantly reduced errors of the model atmosphere and 25 ocean states through “observation”-constraints by ADA and ODA. The weakly CDA in which both the online ADA and ODA are conducted during the coupled model integration shows smaller errors of air-sea fluxes than the single ADA and ODA, facilitating the future utilization of cross-covariance between the atmosphere and ocean at the air-sea interface. A three-year CDA reanalysis experiment is also implemented by assimilating Ps, SST and ocean temperature and salinity profiles from the 30 real world spanning the period 1978 to 1980 using 12 ensemble members. Results show that Ps RMSE is smaller than 20CR and SST RMSE is better than ERA-20C and close to CFSR. The success of the online CESM-ECDA system is the first step to implement a high-resolution long-term climate reanalysis once the algorithm efficiency is much improved.

1 Introduction

The Community Earth System Model (CESM) is a fully coupled global Earth system model developed by the National Center for Atmospheric Research (NCAR), consisting of several geophysical component models (atmosphere, ocean, land, land ice, sea ice, river runoff, and ocean wave) and a central infrastructure for coupling component models. It can simulate the past, present, and future climate states of the Earth system (e.g., Chiodo et al., 2016; Glotfelty et al., 2017; Chang et al., 2020), and has been used worldwide in numerous climate studies (e.g., Goldenson et al., 2012; Cheng et al., 2014; Gantt et al., 2014; Fasullo & Nerem, 2016) to study the evolution mechanisms of climate and environment (e.g., Goosse & Holland, 2005; Bitz, 2008; Chandan & Peltier, 2018), the impact of natural processes and human activities on climate change, and the prediction of climate change (e.g., Coelho & Goddard, 2009; Arblaster et al., 2011; Asefi-Najafabady et al., 2018).

Developing coupled data assimilation (CDA) is an inevitable requirement to improve initialization, state estimation, and prediction of coupled models with observations available in multiple components of the Earth system (Zhang et al., 2020b). Traditionally, data assimilation (DA) is carried out independently in an uncoupled model, such as assimilating atmospheric observations into an atmosphere component model or assimilating oceanic observations into an ocean component model, which is referred to as uncoupled DA (Derber & Rosati, 1989; Rosati et al., 1997; Saha et al., 2006; Balmaseda & Anderson, 2009). When the uncoupled DA is used to initialize the coupled model integration, it is necessary to first combine the single component analyses obtained independently from the single component DA to form the coupled initial conditions for the coupled model. With the wide application of coupled models in the study of weather and climate systems, the demand for CDA is rising rapidly (Penny et al., 2017). CDA refers to the joint assimilation of observations in different component systems and allows to transfer and exchange observational information among different components dynamically and statistically (e.g., Lu et al., 2015; Sluka et al., 2016; Zhang et al., 2020b). It has been shown that CDA is able to improve the interannual climate prediction skills of coupled models (e.g., Collins, 2002; Zhang et al., 2010b). Therefore, CDA is considered as an effective method for the initialization of multi-component coupled Earth system models and the production of coupled reanalysis (Zhang, 2011).

As described by Penny et al. (2017), CDA can be broadly categorized into two approaches: weakly CDA (WCDA) and strongly CDA (SCDA). WCDA is defined by the fact that the coupling occurs during the forecast stage by using a coupled forecast model as DA is ongoing. WCDA assimilates the observations into the corresponding single model component of the coupled model system and then transfers the observational information to other model components through flux exchange of the coupled model. The second approach, SCDA, uses the cross-covariance of model components to directly assimilate the observation of an earth system component into other coupled model components. The advantage of SCDA is that observations at a given time have instantaneous impacts across all components during all available analyses (Penny et al., 2017; Zhang et al., 2020b). Due to the difficulties in obtaining a high signal-to-noise ratio of the covariance between model components (Han et al., 2013), by now the WCDA is still the common choice for assimilating observations into coupled models (e.g., Laloyaux

65 et al., 2016; Browne et al., 2019; Skachko et al., 2019; Tang et al., 2020; Mu et al., 2020) and in the meanwhile some studies have also discussed the SCDA (e.g., Negar et al., 2020). In this study, we use WCDA.

According to the mode of data transfer between the numerical model and assimilation algorithm, ensemble-based CDA can be divided into two categories: offline CDA and online CDA. In offline CDA, data are transferred between the model ensemble and assimilation algorithm through data reading/writing. The data assimilation research testbed (DART, Anderson et al., 2009) 70 developed by NCAR and the Gridpoint Statistical Interpolation (GSI) ensemble Kalman filter (EnKF) system (Kleist et al., 2009) released by the Developmental Testbed Center (DTC) are both based on an offline mode. Although the offline CDA is a convenient way to implement a CDA procedure on a relatively short scale, and the majority of the I/O cost in DART is low compared to the total time (Karspeck et al., 2018), an online CDA system is more efficient and necessary for climate studies. The online CDA is usually realized by integrating a numerical model and DA algorithm into one executable program, so that 75 data exchange between model and assimilation is generally realized by memory management. For example, the ensemble CDA (ECDA) system developed by Zhang et al. (2005 & 2007) based on the Geophysical Fluid Dynamics Laboratory (GFDL) coupled climate model and the Parallel Data Assimilation Framework (PDAF) developed by Nerger et al. (2005 & 2013) based on the fully coupled Alfred Wegener Institute, Helmholtz Center for Polar and Marine Research Climate Model (Mu et al., 2019; Nerger et al., 2020) are online CDA systems.

80 Extensive offline DA works with CESM have been explored in previous studies (e.g., Anderson et al., 2009; Raeder et al., 2012; Karspeck et al., 2013 & 2018). All these studies are based on an offline DA framework which needs to read and write restart files at every assimilating timestep. This time-consuming way makes it difficult to produce a long-term climate reanalysis. In order to develop coupled prediction and climate reanalysis, especially toward the goal of high-resolution CESM (CESM-HR, Zhang et al., 2020a) CDA for HR coupled model prediction initialization and reanalysis, a continuous CDA 85 within CESM is highly desirable, although the DART exists and the next-generation DA system (Joint Center for Satellite Data Assimilation JEDI DA system) is designed and has been developing to replace the GSI and other US agency DA systems. This paper serves as a documentation for the initial step of CESM-HR CDA development, the CESM-ECDA system design and its performance.

In the filtering algorithm, the DA method used in this study (which is ensemble adjustment Kalman filter, EAKF) is the same 90 as previous studies (Zhang & Anderson, 2003; Anderson et al., 2009; Karspeck et al., 2018), but we implement the CESM-ECDA as an online CDA system which uses the computer memory management to realize compiling the assimilation codes and the model codes into an executable file. Avoiding frequent huge data reading/writing is extremely important to realize efficient climate reanalysis especially for high resolution model cases. Although a lot of CESM DA work using DART has been done and a 12-year reanalysis has been presented (Karspeck et al., 2018), longer-term climate reanalysis is still a challenge. 95 Our motivation is to develop an online CESM-ECDA system that can support long-time integration and assimilation in the near future. By that, we can make a series of long-time scale (such as 40-year, or even 100-year) climate reanalysis experiments in different resolutions for climate assessment. This study is different from Karspeck et al. (2018) in the following two aspects:

1) The CESM-ECDA system passes data through memory instead of files, 2) The online DA system within SE dynamic-core atmosphere model can support high-resolution simulation.

100 This paper is organized as follows. Section 2 describes the CGCMs (Coupled General Circulation Model) used in this work, the ensemble filtering algorithm, and the perfect twin experiment design for the evaluation. The implementation of the ensemble-based online CESM DA capability is described in section 3. More specifically, section 3.1 describes the ADA system within the Community Atmosphere Model (CAM) model using the finite-volume dynamical core (dynamic-core; hereafter CAM-FV), section 3.2 describes the ADA system within CAM using the spectral-element dynamic-core CAM (hereafter CAM-SE), section 3.3 discusses the ocean DA (ODA) system with the Parallel Ocean Program (POP) model. Section 4 describes the establishment and evaluation of online CESM-ECDA system. Finally, summary and discussions are given in section 5.

2 Model and Filtering Algorithm

2.1 Brief Description of CESM

110 The version of CESM used in this work is not the latest version of CESM2 (Danabasoglu et al., 2020), but based on an earlier version tagged as CESM1.3-beta17_sehires38, which is a version specifically developed to better support high-resolution CESM simulations (Small et al., 2014; Chang et al., 2020). The corresponding component model versions are the CAM version 5 (CAM5; Neale et al., 2012), the POP version 2 (POP2; Smith et al., 2010), the Community Ice Code version 4 (CICE4; Hunke & Lipscomb, 2008), and the Community Land Model version 4 (CLM4; Lawrence et al., 2011).

115 2.2 Brief Summary of EAKF

The ensemble adjustment Kalman filter (EAKF) was first designed by Anderson (2001) followed by some modifications (Anderson, 2003) and immediately applied to comprehensive general circulation models (Zhang & Anderson, 2003; Zhang et al., 2005 & 2007). As a popular variant of the traditional ensemble Kalman filter (EnKF; Evensen, 1994 & 2003), the EAKF has been widely used in DA research and applications. Compared with the traditional EnKF that randomly perturbs the 120 observations, the advantage of EAKF is that it can retain the higher-order moments (i.e., nonlinear information) in the prior samples (Zhang & Anderson, 2003). The EAKF does not need to perturb observations, thus avoiding the generating of extra noise into the analysis system. Based on a systematic analysis of the existing ensemble filtering algorithms, Tippett et al. (2003) pointed out that the EAKF method is one realization of the ensemble square root filter (EnSRF) and a deterministic filtering algorithm. When the error distribution of each scalar observation is independent of each other, a sequential filtering method 125 can be used to assimilate each scalar observation one by one. When the observation errors are correlated, the singular value decomposition (SVD) can be used to first decorrelate the errors, and then the sequential filtering can be carried out.

As a sequential filter, the EAKF can be conveniently implemented by two steps consisting of two key equations (Anderson, 2001 & 2003; Zhang & Rosati, 2010a). The first equation computes the observational increment Δy_i^0 as

$$\Delta y_i^o = \frac{\frac{1}{(\sigma^p)^2} \bar{y}^p + \frac{1}{(\sigma^p)^2} y^o}{\frac{1}{(\sigma^p)^2} + \frac{1}{(\sigma^o)^2}} + \frac{\Delta y_i^p}{\sqrt{1 + (\frac{\sigma^p}{\sigma^o})^2}} - y_i^p, \quad (1)$$

130 where i is the ensemble index, y represents the observable state variable, and σ is the error standard deviation. The superscript $p(o)$ always denotes the prior quantity estimated by the model (i.e., the observational quantity), and the overbar denotes the ensemble mean. The first term on the right hand is the adjusted ensemble mean, and the second term with the third term on the right hand is called the adjusted ensemble spread.

135 The second step regresses the observational increment onto the relevant model grids, which is computed by the first step. That can be expressed as

$$\Delta x_i^u = \frac{\text{cov}(\Delta x, \Delta y)}{\sigma_y^2} \Delta y_i^o, \quad (2)$$

where $\text{cov}(\Delta x, \Delta y)$ is the covariance and σ_y is the standard deviation, which are both evaluated by the model ensemble. Once all observations are looped over all the relevant model variables on the model grids, the analysis step is completed, and the model is initialized for the integration of the next step. For more details, please refer to Zhang and Rosati (2010a).

140 2.3 Twin Experiment Design

The implementation of CDA is a complex multi-task problem, which involves many factors, such as the coupled model bias, sampling of the observation system and verification of the analysis scheme. The uncertainty in any of these aspects may make the evaluation of a CDA system very difficult. In order to reduce the uncertainty and the evaluation complexity, a perfect model framework based on pseudo-observations (i.e., the perfect twin experiment) is adopted here to eliminate the influence 145 of model bias and observation system sampling on the assessment of the CDA system. The advantage of the perfect twin experiment design is that the known ‘truth’ can be used as an accurate and reliable reference in evaluating the analysis quality of the CDA system. Similar framework has been used in Browne and Leeuwen (2015) to assess the performance of the equivalent weights filter within a coupled ocean–atmosphere general circulation model. In addition, when new assimilation components or observation types are added into the CDA system, the change of the assimilation performance can be effectively 150 quantified.

In the perfect twin experiment design, a time series of single-member model states are taken as the ‘truth’, which can start from an arbitrary date (e.g., denoted as January 1980 in this paper). White noise is then added onto the ‘truth’ to generate the pseudo-observations assimilated in the analysis stage. Thus, the assimilated observations here are gridded data at the grid points as the model variables. The added white noise is a parameter that determines the intensity of the observational constraint.

155 It is used to account for the random measurement error of the observation system, but does not include the representation error reflecting the limitation of the sampling scale. To sufficiently decorrelate the ‘truth’ and the free integration of the model ensemble (i.e., the control experiment without assimilation of any observations), we use the restart of a 20-model-year free integration as the initial condition of the experiments.

The surface pressure reflects the total air mass of the atmosphere column at a location on the Earth's surface (terrain or ocean).

160 Previous studies (e.g., Whitaker et al., 2004; Anderson et al., 2005; Compo et al., 2006) have emphasized several advantages of using surface pressure observations to produce historical reanalyses. As described in Compo et al. 2006, the surface pressure information through geostrophy can be expected to yield a reasonable approximation to the barotropic part of the flow, which accounts for a substantial part of the total flow. There are usually two approaches to implement surface pressure assimilation. One is projecting the observational surface pressure increments to three-dimensional atmospheric variables through the 165 geostrophic relationship (Poli et al., 2016). The other is using the ensemble covariance between the surface pressure and other atmospheric variables to make three-dimensional atmosphere adjusted (e.g., Compo et al., 2011; Yang et al., 2021). The Twentieth Century Reanalysis (20CR) is the first centurial reanalysis to only assimilate surface pressure observations (Compo et al., 2006). Since then, other reanalysis products are generated by assimilating mainly surface pressure observations, such as ERA-20C (Poli et al., 2016), 20CRv2c (Compo et al., 2011), 20CRv3 (Slivinski et al., 2019), and GFDL's DCIS (Yang et al., 170 2021).

Using the covariance of surface pressure to adjust three-dimensional atmospheric variables can increase the observational constraint from surface pressure (Yang et al., 2021), but it often requires a large ensemble size. Here, in order to make the assimilation algorithm more portable and suitable for future high-resolution data assimilation, and considering the development feasibility and efficiency with finite computational resource, we use 12 ensemble members instead of a very large ensemble 175 size as used in 20CR. Such small size ensemble may not be suitable to resolve 3-dimensional increments of atmospheric variables via the ensemble covariance with surface pressure observation. Although we only assimilate the surface pressure, other 3-dimensional variables are also adjusted through geostrophic relationship and thermal wind relationship. Further justification will be provided in Section 4.2.

180 The observation assimilated by ADA is surface pressure (P_s), and the standard deviation of the added observation error is 10 hPa; the observations assimilated by ODA are sea surface temperature (SST), three-dimensional temperature and salinity from *in situ* ocean profiles which are generated from the 'truth'. The corresponding standard deviations of observation errors are 0.5 K for temperature and 0.1 PSU for salinity at the sea surface (typical error levels for SST and sea surface salinity) and exponentially decay to one tenth of the surface values at 2000 m depth. These standard deviations have been trialed and adopted in the previous similar studies (e.g., Zhang et al., 2007). The *in situ* ocean profiles are sampled using the real locations of Argo 185 data in 2007.

The ADA assimilation frequency is 6 hours and the ODA is 1 day. As an initial verification of the CESM-ECDA system, we did not directly use a high-resolution experimental setup, but used a standard resolution [100 km in ocean + 200 (100) km in FV (SE) atmosphere]. Following previous studies (Zhang et al., 2005 & 2007) on covariance localization technique, and under computational resource constraint, trials and errors are used to determine the ensemble size to be 12 in this perfect model study.

190 And the ensembles of initial conditions are constructed using the atmosphere states of 12 consecutive days.

Referring to the 20CRv2 (Compo et al., 2011), CFSR (NCEP Climate Forecast System Reanalysis, Saha et al., 2010) and CM2.1-ECDA (Zhang et al., 2007), the horizontal localization radius is 2000 km in FV core and 2500 km in SE core in ADA in this work.

195 Referring to Zhang et al. (2007) and Kaspeck et al. (2018), the horizontal localization radius of SST observations is set to be 1000 km in ODA. In the vertical direction, SST observations are allowed to affect the ocean temperature of the 10 topmost model levels (100 m depth). The horizontal localization radius of profiles temperature is 1000 km and the salinity is 500 km. In addition, the horizontal correlation scale is multiplied by a $\cos(\theta)$ (θ is the grid latitude) factor up to 80°N (S) to make the scale consistent with the characteristics of the Rossby deformation radius for a global analysis scheme (for more details, please 200 see Zhang et al., 2005 & 2007). Each observation is only allowed to impact at most two neighboring levels (one above and one below), and the deepest profiles layer corrects the model values of all layers below.

The design of the evaluation experiments for the ADA, ODA and CDA is shown in Table 1. Given that our main purpose is to document the development of the online CDA system for the community rather than provide reanalysis products, and the constraint of computational resource, we only ran one model year to verify the reliability of the algorithm in this perfect twin 205 experiment. We can see that the DA in atmosphere and upper ocean has sufficiently converged. The ensemble experiments include the control experiment (ctl) without assimilating any observations, the ADA experiment which only assimilates the P_s observations with CAM-FV (ada_fv) and CAM-SE (ada_se), the ODA experiment assimilating only the SST observations (oda_sst) and both the SST and *in situ* ocean profiles of temperature and salinity (TS profile; oda), and the CDA experiment assimilating both the P_s and SST observations with CAM-FV (cda). The experiments' component setting in this study is 210 BHISTC5 in FV and B1850CN in SE.

The validation of assimilation results is based on the root mean square error (RMSE), which is the most widely used statistic in system evaluation. RMSE is the standard deviation of the prediction errors, which measures how much the simulated data differ from the reference data (i.e., the 'truth'). Since both atmosphere and ocean observations assimilated in this paper are located near the air-sea interface, and in principle, CDA can make more effective use of the observations near the interface 215 and thus improve the coupled state estimation there, this paper mainly analyzes the model variables and fluxes near the interface. The atmosphere model variables near the interface used in this paper include the atmosphere surface pressure (P_s), surface temperature (T_s), surface wind components (U_s and V_s) and surface specific humidity (Q_s). The analyzed ocean model variables include SST and ocean subsurface temperature and salinity. The fluxes at the air-sea interface used here include the sensible heat flux (SHF) and the latent heat flux (LHF).

220 **3 Development of Online DA Components of CESM**

This section describes the framework and implementation of the online DA components of the CESM-ECDA system, which include the ADA component with CAM and the ODA component within POP. The ADA components are implemented to both CAM-FV and CAM-SE.

3.1 ADA with CAM-FV

225 **3.1.1 Online Ensemble Collection-distribution with CAM-FV Data Structure**

CAM-FV adopts regular latitude-longitude grid in the horizontal direction, and both the model and assimilation are performed in parallel modes. The parallel domain decomposition in the model integration space is realized by dividing the global field in the horizontal direction based on the adjacent geophysical location. During the forecast stage, each processing element (PE) is responsible for a sub-domain of the global field of a single ensemble member, and different ensemble members are completely 230 independent when the model integrated forward. When the model ensemble reaches the analysis time, a “super-parallel” technique (Zhang et al., 2007) is used to transmit the data between the model space and the analysis space. The super-parallel technique allows to make full use of the available computing resources and makes the model integration and the analysis be carried out online in an iterative manner.

Online data interaction based on the super-parallel technique mainly includes two stages: online ensemble collection and online 235 ensemble distribution. Online collection refers to the transformation of the parallel domain decomposition and corresponding data storage form of the model space to those of the analysis space. As a result, each PE can obtain the ensemble data required by the ensemble filtering algorithm. On the contrary, online distribution indicates the transformation of the domain decomposition and data storage form of the analysis space back to those of the model space. In this way, the updated analysis ensemble can be used as the initial conditions for the model integration of the next assimilation cycle. The transformation 240 between the model space and the analysis space is mainly based on the data collection and distribution functions of the Message Passing Interface (MPI; Gropp et al., 1996), and it is an online data interaction mode via the memory-based reading/writing. An online coupling strategy and implementing standards using MPI into an ensemble data assimilation system has been detailed in Browne and Wilson (2015).

Figure 1-a is an example of the parallel domain decomposition and online collection and distribution with a total of 16 PEs 245 and 4 ensemble members with CAM-FV. In order to conduct the parallel task decomposition in the analysis space, the global field is divided onto K PEs of the global PE list. To some extent, the parallel decomposition in the analysis space is arbitrary, while **Figure 1-a** just shows a global domain decomposition according to a layout with 4×4 PEs. It should be noted that we can also specify other decomposition layout types, such as 2×8 PEs etc. The halo is 12 grids in our experiments. In theory, the halo should depend on the localization scale. But practically, we choose an appropriate halo according to some previous 250 experiments and model resolutions.

3.1.2 Implementation of Sequential EAKF Algorithm with CAM-FV

The implementation of the sequential EAKF with CAM-FV uses an approximate algorithm of the compute-domain/data-domain strategy of Anderson (Anderson, 2001) to parallelize the filter. **Figure 2** shows a schematic of the implementation of the sequential EAKF algorithm with CAM-FV. The algorithm assumes that the observations will only impact the “nearby” model grids. Here “nearby” is generally defined by two conditions. One is that the nearby model grids must be located on the current PE; the other is that the use of localization scheme requires that the nearby model grids should be within the localization radius of the current observation. In the analysis space, the global field is divided into a group of analysis core domains (i.e., compute domain, see **Figure 1-a**) in the horizontal direction. Each core domain is surrounded by a certain number of nearby grids, which are referred as halo (see **Figure 2**). An analysis core domain and its halo jointly constitutes an analysis domain (i.e., data domain). The analysis process is based on the analysis domain, and each PE is responsible for the assimilation of one analysis domain. When a set of observations are available, the online collection process transforms the required subset of ensemble model states for each analysis domain to the corresponding PE. In each analysis domain, all available observations are assimilated one by one using the EAKF algorithm (see Section 2.2) sequentially.

The ADA system with CAM-FV is realized using the two-step method of EAKF (Anderson, 2003; Zhang & Rosati, 2010) based on the online ensemble collection and distribution processes. As **Figure 1-a** shows, after the online ensemble collection, each PE obtains the ensemble vector of model states for an analysis domain. Then, the observational increment is calculated based on Equation (1) on all PEs in parallel. It should be noted that one observation will be assimilated only if the ensemble of all state variables required for the forward operator calculation is available on the current PE. After the observational increments are obtained, they are projected onto the nearby model states to get the analysis increments via linear regression expressed by Equation (2). Thus, the nearby model states can be updated by this observation via adding the analysis increments onto the background model states. Therefore, the model states used in the assimilation of the current observation have already been updated by all previous assimilated observations. This two-step assimilation process is repeated sequentially for the subsequent observations until all available observations of the current analysis step are processed. Finally, the analysis ensemble in the analysis core domains needs to be converted back to each member model space by online ensemble distribution to be ready for the next integration stage.

3.2 ADA with CAM-SE

3.2.1 Online Ensemble Collection-distribution with CAM-SE Data Structure

Unlike the regular latitude-longitude horizontal grid used in CAM-FV, CAM-SE uses a cubed-sphere grid in the horizontal direction (Dennis et al., 2012; Evans et al., 2013), which is no longer a logically rectangular grid. The direct effect of using such a grid on the form of data storage in the model space is that the model states are no longer represented as two-dimensional variables in the horizontal direction, but are combined into one dimension. Taking the ne30np4 resolution of CAM-SE as an example, the two horizontal dimensions of the model variables in the geophysical space are represented by one dimension of

length 48602 in the array form. Moreover, due to the characteristics of the cubed-sphere grid, two adjacent grid points in the horizontal one-dimensional representation of the variable with CAM-SE may not represent that the two grid points are adjacent in the geophysical space. Therefore, the parallel decomposition strategy of the analysis domain with CAM-FV is no longer applicable to CAM-SE. Because the adjacent model grid points in the geophysical space can no longer be always ensured to be divided and stored on the same PE.

In order to implement the online ensemble collection and distribution with CAM-SE, the model state variables are vectorized. When the model reaches the analysis time, the ensemble of model states is first obtained based on the collection function of MPI. This process is similar to that with CAM-FV, except that the collected state variables are all one dimension less than the same variables with CAM-FV. Then, all state variables of a single ensemble member are converted into a one-dimensional array. In principle, the arrangement of the model grid points in this array can be in an arbitrary order, because the location information of each point will be recorded by a separate array. In this way, the ensemble of all model state variables will be represented by a two-dimensional array, where one dimension corresponds to the grid point sequence number and the other represents the ensemble sequence number. Then, the parallel decomposition of the analysis domain is achieved by dividing the grid point dimension over all PEs. As a result, each PE obtains the information about the ensemble of a subsequence of model state variables. However, it should be emphasized that the grid points in this subsequence in principle can be arbitrarily distributed and are not required to be adjacent in the geophysical space. At this point, the data conversion from the model integration space based on the online ensemble collection to the analysis space with CAM-SE is completed. When the assimilation of all available observations at the current time is completed, the updated analysis ensemble obtained in the analysis space are converted back to the model space. This process is an inverse of the collection procedure and is implemented based on the MPI distribution function. **Figure 1-b** shows an example of the parallel domain decomposition and online collection and distribution with a total of 8 PEs and 4 ensemble members with CAM-SE.

3.2.2 Implementation of Parallel EAKF Algorithm with CAM-SE

The implementation of the ensemble filter with CAM-SE is also based on the two-step EAKF algorithm. Different from CAM-FV, the implementation needs to be adapted to the specific decomposition strategy of the analysis domains with CAM-SE. The differences are mainly in the computation of the observation prior ensemble and the regression of the observational increments. **Figure 3** shows the schematic of the implementation of the parallel EAKF algorithm with CAM-SE.

The computation of the observation prior ensemble with CAM-SE uses the same method as DART (Anderson et al., 2009), which is implemented based on the remote memory access (RMA) technique of MPI2 (Gropp et al., 1999). Because the grid points are divided onto different PEs via an arbitrary way, the four grid points enclosing one observation for interpolation may be located on different PEs from the owner PE of the observation. In the best case, all four enclosing points are located on the same PE as the owner PE; while in the worst case, all four enclosing points are located on four different PEs. Therefore, it needs to obtain the model background from the memories of other PEs (i.e., remote memories) for computing the observation priors. In order to fulfillment this requirement, the RMA technique of MPI2 is used, which allows one PE to read or write

asynchronously the memories of other PEs through a virtual window. Thus, regardless of which PEs the four enclosing points of the observation are located on, the prior ensemble for this observation can be obtained with aids of the RMA technique. Then the observational increment ensemble can be calculated based on Equation (1).

The regression of the observational increments with CAM-SE is based on a parallel implementation of the EAKF algorithm (Anderson & Collins, 2007). With CAM-FV, the observational increments are mapped onto the nearby model grids via linear regression to obtain the analysis increments of the nearby model states. With CAM-SE, the calculation of the observation priors requires access to the remote memories through RMA, which is more complex and computationally expensive than the direct access to the local memory with CAM-FV. To optimize the filtering algorithm with CAM-SE, the computation of the forward observation operator is implemented based on a parallel algorithm of Anderson and Collins (2007). This algorithm is suitable for the parallel implementation of the EAKF algorithm. It splits the traditional forward observation operator computation, executed once for each observation, into a one-time calculation for all observations and an update of the nearby subsequent observation priors which have not been assimilated. Therefore, with CAM-SE, the forward operator computation is executed only once for each assimilation step. In this parallel implementation, the prior ensembles are first computed for all observations using the model background that has not been affected by any observation. Then, when an observation comes in, its observational increments update not only the nearby model states as in CAM-FV, but also the prior ensembles of all nearby observations that have not been assimilated (i.e., the subsequent observation priors). This parallel algorithm has been shown to produce identical results to the traditional sequential algorithm. More details of this parallel implementation can be found in Anderson and Collins (2007).

3.3 ODA with POP

The online collection and distribution processes with POP are similar to those with CAM-FV (**Figure 1-a**). Although the horizontal grid used in POP is different from the regular latitude-longitude grid in CAM-FV, they both belong to the logically rectangular grid. More specifically, the horizontal dimensions of model variables can be represented by latitude and longitude. Therefore, similar parallel domain decomposition strategy based on the geophysical space to that with CAM-FV is used with POP to obtain the analysis domain. With CAM-FV, the decomposition of the analysis domains is based on the global horizontal field. While with POP, the analysis domain decomposition is further optimized via a so-called local secondary decomposition on the model integration domain. In this local secondary decomposition strategy, the same model integration domains of all ensemble members are directly decomposed onto the PEs responsible for the integration calculation of these integration domains of all ensemble members. Taking **Figure 1-a** as an example, the southwest (i.e., lower-left) integration domains of 4 ensemble members are decomposed onto PEs 0, 4, 8, and 12 to obtain the analysis domains. Because the collection of the entire global field of model states can be avoided (replaced by the collection of a subset of the global field), thus this local secondary decomposition strategy with POP reduces the hard limit on the PE storage capability. However, it should be pointed out that one disadvantage of this decomposition method is that the halo width in the analysis domain cannot exceed that of the

integration domain. The implementation of the sequential EAKF algorithm with POP is the same as that of CAM-FV (see **Figure 2**), thus not repeated here.

350 3.4 The Online CESM-ECDA System

When the DA systems in CAM and POP have been developed respectively, the ocean-atmosphere CESM-ECDA system can be constructed. **Figure 1-c** shows the implementation framework of the CESM-ECDA system. In one assimilation cycle, the execution of CESM-ECDA system can be described as follows. The CESM model reads in the initial condition ensemble to start the forward integration of the model ensemble. When the model integration reaches the observation time, the model ensemble integration is suspended. Then the forecast fields of CAM and/or POP are obtained as the background fields of the assimilation by the ADA and/or ODA components through the online ensemble collection, then the two-step update of EAKF is used for the sequential assimilation of the observations in each component. After the assimilation process has been completed, the analysis fields obtained by ADA and/or ODA are transformed back to corresponding model spaces through the online ensemble distribution. Then the analysis ensemble updated by the observations is used as the initial states for the model ensemble to continue the integration in the next forecast stage. It should be noted that the ADA and ODA components can be executed using the same or different frequencies. Generally, the ODA interval is longer than that of ADA to account for the different characteristic time scales between the ocean and the atmosphere. Because the background fields used in ADA and ODA come from the atmosphere and ocean components of the coupled CESM, and the dynamic coupling between the atmosphere and ocean components is performed through the interface fluxes in the model forecast stage. The observed information in the atmosphere and ocean can be exchanged with each other, so that the coupled state estimation obtained by the CESM-ECDA is more self-consistent and balanced. In addition, because the coupled covariance between the atmosphere and the ocean is not used in the current CESM-ECDA system, the observation in one component is not allowed to directly update the model state in the other component in the assimilation stage, which makes it a weakly coupled DA (WCDA) system.

4 The Evaluation of CESM-ECDA System with prefer twin experiment

370 4.1 ADA with CAM-FV

The assimilation of P_s observations by ADA with CAM-FV significantly improves the atmospheric surface variables. **Figure 4 (a-e)** shows the time series of RMSEs of five atmospheric surface variables and Table 2 shows the global averaged RMSEs. To focus on the impact of assimilation after the system reaches equilibrium, the globally averaged RMSEs of atmospheric variables and fluxes are calculated with the experiment output data of the first month excluded in this paper. By assimilating P_s observations, not only the surface pressure, but also other atmospheric variables are significantly improved. Compared with the *ctl*, the RMSEs of surface variables are clearly and rapidly reduced by assimilating P_s observations. The global averaged RMSE of P_s is reduced from 6.68 hPa to 4.05 hPa, nearly improved by 40%. The RMSEs of other four variables are reduced by about 15%–25%.

380 **Figure 5 (a-e)** shows the distribution of the ada_fv-to-ctl (hereafter ada_fv/ctl) RMSE ratio of the five atmospheric surface variables. Compared to ctl, which does not assimilate observation, the assimilation of P_s in ada_fv can significantly reduce the RMSE of P_s all over the globe. The RMSEs of U_s and V_s are also reduced throughout the globe in ada_fv. Though the RMSEs of T_s and Q_s are increased in some regions in ada_fv, the assimilation of P_s observations can improve the analysis accuracy over most regions. Besides, the improvements are mostly located at the mid-latitudes on both hemispheres, especially in the south hemisphere. P_s is a two-dimensional variable, but it contains abundant three-dimensional information of the atmosphere.

385 Therefore, the solo assimilation of P_s observations not only significantly corrects the model P_s field, but also improves other atmospheric variables. It should be pointed out that U , V , T and Q are not used as direct assimilating variables, but are adjusted through the dynamic process and physical process of the model after assimilating P_s . And the errors of these variables are also significantly reduced, which shows that the assimilation effect of the system in the model is reasonable.

4.2 ADA with CAM-SE

390 The atmospheric surface variables by assimilating the P_s observations within CAM-SE are also significantly improved. **Figure 6 (a-e)** shows the time series of RMSEs of five atmospheric surface variables and Table 3 shows the global averaged RMSEs. The calculation of the global averaged RMSEs also excludes the output data of the first month. Generally speaking, the assimilation effects of P_s observations with CAM-FV and CAM-SE are similar. The ADA system with CAM-SE can also significantly improve the atmospheric variables over the ctl experiment, even only the P_s observations are assimilated.

395 Furthermore, the amplitude of the RMSE reduction with CAM-SE tends to be smaller than that with CAM-FV, especially for P_s , U_s and V_s (Table 2 vs. Table 3). For example, compared with the ctl experiment, ada_fv reduces the RMSEs of P_s , U_s , and V_s by up to 39.4%, 25.5%, and 26.1%, respectively, while the corresponding RMSE reductions in ada_se are 29.4%, 20.1%, and 17.0%, respectively. In addition, the horizontal distribution of RMSE in SE (not shown here) is similar to that in FV.

400 **Figure 7 (a-f)** shows the time series of RMSEs of upper layer atmospheric variables, being temperature and winds at 870 hPa and 510 hPa as examples. The RMSEs of all these three variabilities in ada_se are also smaller than that in ctl experiment in high-level atmosphere. At 870 hPa level, the RMSEs of temperature, zonal wind and meridional wind from ctl are 3.43 K, 6.18 m/s and 5.45 m/s. After assimilating the only surface pressure, these RMSEs are decreased to 3.02 K, 4.99 m/s and 4.64 m/s respectively. At 510 hPa level, the RMSEs from ctl are 3.32 K, 8.72 m/s and 8.01 m/s, while the RMSEs from ada_se are 3.00 K, 7.72 m/s and 7.24 m/s respectively. The model errors of other atmospheric variables are also reduced, which will not be displayed one by one here. It is worth to mention that the reduction rate of RMSEs for the variables in the upper layers is much smaller than that in the surface. This might suggest that the simultaneous increments of 3-dimensional winds, temperature and moisture are very important for representing the atmosphere state in the whole troposphere (Yang et al., 2021). When there are enough computing resources in the future, we will consider increasing ensemble size to assimilate three-dimensional atmospheric variables to further improve results.

410 One aspect of surface pressure data assimilation shown in 20CR is that it could have very similar weather-to-climate scale
variability in the troposphere as other traditional atmosphere reanalyses which use all available observations. **Figure 8-ab**
shows the distribution of anomaly correlation coefficient (ACC) between ctl (ada_se) and ‘truth’ in 500-hPa geopotential
height. The ACC between ctl and ‘truth’ is about 0.6 ~ 0.9 in Eurasian continent and about 0.5 ~ 0.7 in North America
(Fig. 8a). In North Pacific and North Atlantic, the maximum ACC of ctl and ‘truth’ is about 0.8 and the minimum is
415 about 0.3. In the southern hemisphere, the ACC of ctl and ‘truth’ is much smaller than that in the northern hemisphere.
For example, in the south of 30 °S, the ACC of ctl and ‘truth’ are below 0.4 in the Southern Ocean. It may be related to
the large simulated interannual variability of CESM in the southern hemisphere since we use the results of CESM in
another year as truth. Globally, the areas with the smallest ACC are the equatorial Pacific and the equatorial Indian
420 Ocean, ctl and ‘truth’ are basically negatively correlated, which may be related to the high-frequency motions in the
equatorial region. The ACC of ada_se and ‘truth’ increases significantly after assimilation (**Fig. 8b**). The maximum
value of ACC in Eurasian continent can reach 0.9 ~ 1.0, and the ACC also increases significantly in North America,
Southern Ocean, equatorial ocean and other regions. **Figure 9a** shows the time series of 500-hPa geopotential height
RMSE. Compared with ctl, the RMSE of ada_se significantly reduces. It can be considered that the weather variability in
the middle troposphere is retrieved by the surface pressure data assimilation.
425 **Fig. 8-cd** show the distribution of ACC between ctl (ada_se) and ‘truth’ in 300-hPa geopotential height. The ACC between
ctl and ‘truth’ in the northern hemisphere is higher than the southern hemisphere, which is similar to 500 hPa. The
northern hemisphere is basically above 0.5, and the southern hemisphere is below 0.4 except for areas around 30 °S. The
ACC in the equatorial region is also relatively low, which is similar to 500 hPa. After assimilating the surface pressure,
the result of geopotential height at 300 hPa is obviously improved. The ACC increases all over the world. For example, the
430 ACC is about 0.7 ~ 0.9 in northern hemisphere continent and about 0.2 ~ 0.5 in the Southern Ocean. **Fig.9b** shows the time
series of 300-hPa geopotential height RMSE. Compared with ctl, the RMSE of ada_se significantly reduces which is
similar with 500 hPa. It can be considered as the evidence that the weather variability in the upper troposphere is adjusted
through the dynamic process and physical process of the model after assimilating surface pressure.

4.3 ODA

435 4.3.1 Assimilation of SST

The assimilation of SST observations by the ODA system with POP significantly improves the accuracy of the ocean states.
Figure 10(a-b) shows the time series of RMSE of SST from ctl and oda_sst, and the distribution of the oda_sst-to-ctl (hereafter
oda_sst/ctl) RMSE ratio of SST. To focus on the impact of assimilation after the ocean system reaches equilibrium, the global
averaged RMSE and the RMSE ratio of the oceanic variables are computed with the output data in which the first three months
440 were excluded in this paper. Compared with the ctl experiment, the RMSE of SST in oda_sst significantly and quickly reduces

at the beginning of the experiment, and then gradually decreases further and stays stably. The SST RMSE in oda_sst reduces from 0.58 K to 0.13 K. The distribution of the RMSE ratio (oda_sst/ctl) shows that the oda_sst experiment can improve the quality of SST over almost the entire globe, except in the high-latitude regions of the north hemisphere. Besides, the distribution of the improvement in oda_sst is relatively uniform compared with that in the ADA experiments discussed above.

445 By assimilating SST, the RMSE of SST is significantly reduced, which is consistent with previous studies such as CFSR (Saha et al., 2010).

4.3.2 Assimilation of *in situ* Ocean Profiles

The design of the assimilation of *in situ* ocean profile temperature and salinity observations with POP is similar to the EAKF algorithm of CM2.1-ECDA (Zhang et al., 2007). Since the locations of the real profile observations are changing over time

450 and they are not coincident with the model grid points. The first step of profile assimilation is to get the model values at the positions of profiles by interpolating and then calculating the observational increment. When calculating the observational increment, eight-points interpolation is used, that is, both the upper and lower four points are used for the interpolation to obtain the model value at the observational point. The second step is to project the observational increment onto the surrounding model grid points. In the vertical direction, each profile affects one layer above and one layer below, with a total
455 of two model layers. Same as the previous study (Zhang et al., 2007), the impact from temperature to salinity and the impact from salinity to temperature are both activated. In accordance with the SST assimilation, the frequency of profile observations assimilation is also 1 day. The distributions of the profile observations are shown in **Figure 11(a-d)**.

The addition of ocean profile observations to the ODA system further significantly improves the ocean state estimates over the control run. **Figure 12 (a-d)** shows the time series of RMSEs of ocean temperature and salinity vertically averaged from 0

460 – 500 m and 500 – 2000 m from the ctl and oda experiments. And Table 4 shows the global averaged RMSEs of these four variables, with the data of the last six months. Compared with the ctl experiment, the RMSEs of temperature and salinity are both significantly reduced. Assimilation of temperature and salinity profile observations rapidly reduces the RMSE compared to ctl at the beginning of the experiments in 0 – 500 m. Compared with the salinity, the RMSE of temperature decreases more rapidly to a stable level (approximately 3 – 4 months for the temperature vs. 7 – 8 months for the salinity). Besides, at the same
465 depth range, the improvement to the temperature tends to be larger than the salinity, with the RMSE reduction of 25.0% (9.9%) and 7.1% (1.2%) for the 0 – 500 m (500 – 2000 m) temperature and salinity, respectively. And for the same variable, the reduction of RMSE in the shallower ocean is larger than the deeper ocean (Table 4), which may be caused by the slower variability of the deeper ocean.

Compared with ctl, oda greatly improves the ocean temperature and salinity estimates, especially in the shallow ocean (0 –

470 500 m). The RMSEs of ocean temperature and salinity are clearly reduced in most regions of the globe between the surface and 500 m depth, in addition to the coast of Africa and the high latitude areas of the North Pacific. The largely improved regions are mostly located in the low- to mid-latitude regions, especially in the Pacific and Indian Oceans. In the deeper ocean (500 – 2000 m), the improvement of temperature and salinity is less significant than in the upper ocean, showing a small RMSE

reduction from ctl compared to the upper ocean. Overall, the improvement of salinity is smaller than temperature. This method
475 of improving ocean model state estimate by assimilating temperature and salinity profiles has also been applied in previous studies, such as Zhang et al. (2007) and Carton et al. (2018). The conclusion in this work is basically consistent with them.

4.4 CDA

After the ADA and ODA components have been implemented based on CAM and POP, respectively, the CESM-ECDA system is also constructed. Because the ocean-atmosphere coupled error covariance is not used in the CESM-ECDA system, the
480 observation in one component system (such as the atmosphere) cannot directly affect the model state in another component (such as the ocean) in the analysis stage. Therefore, the CESM-ECDA system is implemented in the WCDA style. In the current version of the CESM-ECDA system, the ADA component is capable of assimilating the atmospheric observations of the two-dimensional surface pressure, the three-dimensional temperature, wind components and humidity; and the ODA component can assimilate the oceanic observations of the two-dimensional SST and the three-dimensional *in situ* profiles of
485 temperature and salinity. Besides, the localization, covariance inflation and incremental analysis update (IAU; Bloom et al., 1996) schemes are also included. More specifically, the localization schemes include the variable localization, horizontal localization and vertical localization based on the widely-used filter from Gaspari and Cohn (1999), and the covariance inflation is applied with both the classic scheme from Anderson and Anderson (1999) and the relax-to-prior scheme (Zhang et al., 2004).

490 4.4.1 Impact of CDA on Atmosphere State Estimation

The CESM-ECDA system can improve the quality of the atmosphere state estimation over the single ADA experiment. When the assimilation of P_s observations in the atmosphere and SST observations in the ocean are both activated, the CDA system operates in a WCDA style (i.e., the cda experiment). Compared with the single ADA experiment, the cda experiment can be used to evaluate the assimilation performance of the CESM-ECDA system in the atmosphere. **Figures 13 (a-e)** show the time
495 series of RMSEs of five atmospheric surface variables. When the P_s and SST observations are both assimilated, the cda experiment can further reduce the RMSEs of the atmospheric variables in comparison with the ada_fv experiment, which only assimilates the P_s observations into the atmosphere.

Table 5 lists the global averaged RMSEs of these five variables and three important air-sea interface fluxes with the data. Although the cda experiment can improve all the atmospheric surface variables considered here over ada_fv, the error
500 reductions are small (approximately 1% – 2%, and the T_s is 4.3%). This may be caused by the strong correlation between the ocean temperature and atmosphere temperature near the air-sea interface, while the correlation between SST and other atmospheric surface variables is weak. Compared with ada_fv, the cda experiment further includes the assimilation of SST observations into the ocean component. Therefore, the model SST state is well constrained by the SST observations. The improved SST in cda can further benefit the overlying atmosphere through the ocean-atmosphere dynamic coupling. Although

505 all atmospheric states should be improved by the better lower boundary conditions provided by the ocean, only those strongly correlated with the SST more significantly benefit from the improved SST.

The cda experiment shows a mixed distribution of decreased and increased RMSE and a global averaged weak improvement for P_s , Q_s , U_s , and V_s . The regions of significant improvement are mostly located in the tropical eastern Indian Ocean and the tropical to subtropical Atlantic, which may indicate the more significant positive impact of the coupling between SST and air-sea fluxes. It should be noted here that the cda experiment can significantly improve the T_s state over almost the entire ocean areas, especially in the tropical Indian Ocean, the tropical to subtropical Atlantic, and the mid-latitude Pacific.

510 The improvement of CESM-ECDA over single ADA experiment can also be reflected in the air-sea interface fluxes. **Figure 14 (a-d)** show the time series and ratio (cda/ada_fv) distribution of RMSEs of SHF and LHF. These fluxes can also be improved by the further assimilation of the SST observations into the ocean in the cda experiment. Compared with ada_fv, cda further 515 reduces the RMSEs of SHF, and LHF by 3.8%, and 2.1% (Table 5), respectively. These two fluxes share significant improved regions with above variables, such as the tropical Indian Ocean and the tropical to subtropical Atlantic. The assimilation of SST observations in cda improves the air-sea coupling processes in these regions, leading to corrected interface fluxes there. Then the improved interface fluxes further transmit the correcting information to the overlying atmosphere.

4.4.2 Impact of CDA on ocean State Estimation

520 The CESM-ECDA system can obtain improved ocean states over the single ODA experiment. **Figure 14(e-f)** shows the time series and distribution of the SST RMSE from the oda and cda experiments. Compared with oda which only assimilates the SST and profiles observations, cda further assimilates the P_s observations into the atmosphere component. Therefore, the comparison between oda and cda can be used to evaluate the impact of the CESM-ECDA system on the ocean state estimation. Assimilation of SST observations alone in the oda experiment has already largely reduced the SST RMSE in comparison with 525 the ctl experiment. While cda can further reduce the SST RMSE by up to 10.4% (from 0.134 K to 0.120 K, with the data of the first three months excluded from the computation). The RMSE of SST can be significantly reduced in most regions except for the Arctic Ocean by further assimilating the P_s observations into the atmosphere. The SST RMSE in cda decreases about 10%~20% compared to oda. When P_s observations are assimilated into the atmosphere, the atmospheric states are better constrained, which provides an improved upper boundary condition for the ocean.

530 4.5 Computational efficiency of online vs. offline CDA

The data assimilation can be implemented by either an offline or an online mode. In offline, data assimilation and model integration are independently performed in two programs, for which at each assimilation time the model integration needs to stop and write (read) model states on (from) local disks for assimilation (next model integration). In online, data assimilation and model integration are performed in one program, in which the model integration and assimilation are linked by memory 535 management. Both online and offline assimilation modes share model integration and assimilation consumptions, but the

offline mode needs additional I/O and initialization consumptions at each assimilation step. So, their difference of CPU (Central Processing Unit) time mainly depends on the process of initialization and I/O, as well as the assimilation frequency. If at an assimilation interval, the model initialization and I/O time is A, model integration time is B, analysis time is C, the total CPU time in offline and online assimilation is respectively $n \times (A+B+C)$ and $A+n \times (B+C)$ for n assimilation steps. So, the 540 ratio between online time and offline time can be expressed as:

$$R = \frac{\text{online time}}{\text{offline time}} = \frac{A+n(B+C)}{n(A+B+C)} = 1 - \frac{(n-1)A}{n(A+B+C)} = 1 - \frac{n-1}{n} \frac{1}{1 + \frac{B+C}{A}} \quad (3)$$

As n is large enough, $(n-1)/n \rightarrow 1$. The CPU time saved by online assimilation mainly depends on the proportion of $(B+C)$ and A. For example, if $A=B+C$, $R \approx 1/2$; if $A=4(B+C)$, $R \approx 1/5$. By the way, here we only discuss the difference of CPU times in offline and online assimilation modes. However, depending on the performance of HPC (High Performance Computing) 545 system, the I/O process wall clock time may be much longer than the CPU time.

Table 6 presents the comparison of CPU time in offline cda experiments and online cda experiments. We use the resolution of ne30_g16 and the compset of B1850CN for system evaluation. The assimilation frequency is daily in ocean and 6-hourly in atmosphere. The number of observations is same every day. The ensemble size is set to 12 and each member use 32 process (32 tasks, 1 thread). In Table 6, total time mainly consists of initialization time (Init Time) and running time (Run time).

550 It takes about 36m 29s (36 minutes 29 seconds) to run 1-day offline cda, but it only takes about 14m 43s to run 1-day online cda experiment. A 30-day offline cda experiment costs 18h 15m 11s and the online experiment only costs 3h 51m 31s. The CPU time of online assimilation is only 21.14% of offline assimilation. Indeed, a 365-day online cda costs about 20.53% of offline cda time. If the reanalyses over decades are carrying out, the efficiency of online assimilation will be much higher than the offline mode. Again, depending on the performance of HPC system, the I/O process wall clock time may cost much more 555 time through offline assimilation.

5 The real observation assimilating experiment

The results of the perfect twin experiment show that the CESM-ECDA system can work well. To further verify its performance in the real world, a three-year reanalysis experiment (hereafter referred to as real-CDA) from 1978 to 1980 (one-year ODA and two-year CDA) with the component setting of BHISTC5 (historical run with CAM5) is conducted using 12 ensemble 560 members. Surface pressure from ERA-interim (Dee et al., 2011) and grided observational SST from HadISST (Rayner et al. 2003) and three-dimensional temperature and salinity profiles from XBT, CTD, MBT and OSD are assimilated. Considering that observations below 2000 m are very sparse and internal variability in the deep ocean is weak, we employ global restoring of climatological temperature and salinity (e.g., Levitus 2001; 2005; 2012) in the deep ocean to relax the distorted ocean 565 stratification caused by strong data constraint in upper ocean (Lu et al., 2020). A control experiment (real-CTL) is also conducted with the same setup except that it does not employ data assimilation.

We compare the P_s and SST results of real-CDA with those of CFSR (Saha et al., 2010), 20CRv2 (Compo et al., 2011), 20CRv3 (Slivinski et al., 2019), ERA-20C (Poli et al., 2013) and CERA-20C (Laloyaux et al., 2018) in **Figure 15 (a-d)** for 1980. The RMSE of P_s in real-CDA (red line) is smaller than the CTL (black line) and 20CRv2 (yellow) but larger than the CFSR (purple line), ERA-20C (pink line) and 20CRv3 (green line). The mean RMSEs of CTL, real-CDA, CFSR, 20CRv2 and ERA-20C and 20CRv3 are 15.57, 11.84, 9.21, 13.89, 6.68 and 4.82 hPa, respectively. In these reanalysis products, the RMSE of 20CRv3 is smallest if we take ERA-interim as ‘truth’.

The RMSE of SST in real-CDA is smaller than real-CTL (black) and CERA-20C (pink line) and close to CFSR (purple line). The mean RMSEs are 1.41, 0.16, 0.16, and 0.80 °C in real-CTL, real-CDA, CFSR and CERA-20C, respectively. From the distributions (**Fig 15, cd**), we see that the P_s RMSE in real-CDA decrease 30%~50% in the global world compared to CTL in addition to Africa. Compared with CERA-20C, the SST RMSE is greatly reduced worldwide to an extend about 30% ~ 90%. Here, we are not saying that the results of real-CDA are better than CERA-20C, because the SST in CERA-20C is relaxed toward the HadISST2 monthly ensemble product (Laloyaux et al., 2018). The limited results in **Fig. 15** only shows the effectiveness of CESM-ECDA system. More real observation assimilation experiments and more comprehensive verification analysis will be carried out in future work.

580 6 Summary and Discussions

In this paper, an online ensemble atmosphere-ocean coupled data assimilation system within the Community Earth System Model, which consists of the ODA component and the ADA components (both for the finite-volume and the spectral-element dynamical cores for ADA), is designed and evaluated systematically. In the ADA component, the surface pressure observations are assimilated. In the ODA component, the gridded SST observations and the *in-situ* profiles of temperature and salinity are both assimilated. The perfect twin experiments have been conducted steadily for one model year for the single ADA components, the single ODA component, and the weakly coupled CESM-ECDA system. The results show that the CESM-ECDA system is effective in assimilating observations in both atmosphere and ocean. By assimilating the surface pressure observations alone, the RMSEs are significantly reduced by up to 39% for P_s and 16% – 26% for T_s , Q_s , U_s and V_s within CAM-FV. The RMSE reductions for the single ADA experiment within CAM-SE are generally smaller but still significant than those in CAM-FV. By assimilating the SST observations alone, the SST RMSE is greatly reduced by up to 77%. When the three-dimensional *in situ* temperature and salinity profiles are further assimilated in the ODA system, the three-dimensional ocean temperature and salinity can be significantly improved.

When the atmospheric and oceanic observations are jointly assimilated, the CESM-ECDA system executes in a WCDA style. Results show that the CESM-ECDA system can obtain robustly improved state estimations in both atmosphere and ocean compared with the corresponding single component DA experiments discussed above, respectively, which confirms the stability and effectiveness of the established CESM-ECDA system. The atmosphere-ocean coupled assimilation allows to make more effective use of the available observations in both atmosphere and ocean components. Therefore, the observational

information in different component systems is allowed to be transmitted and exchanged across the air-sea interface in the forecast stage of the coupled model. It is worth mentioning that due to the significant difference of the characteristic spatial and temporal scales between the atmosphere and the ocean and the difference of the air-sea coupling mechanisms in different regions, the obtained coupled state estimation shows a more complicated distribution.

This study also introduces and compares the offline and online assimilation approaches. A test which assimilates SST and T&S profiles once a day and Ps four times a day shows that the online assimilation can save about 80% CPU time, which will greatly improve the efficiency of long-term climate reanalysis. Furthermore, the reanalysis experiment with real observations shows that the Ps RMSE of CESM-ECDA is smaller than 20CR if we take ERA-interim as truth. The SST RMSE of CESM-ECDA is smaller than CERA-20C and close to CFSR when HadISST is assimilated.

A previous adaptively inflated ensemble filter study has been designed to enhance the consistency of upper- and deep-ocean adjustments, which is based on “climatological” standard deviations being adaptively updated by observations (Zhang et al., 2010a). But in this study, we only focus on the system design and evaluation of the CESM-ECDA, the inflation is not used in this study. The inflation scheme can be considered into the ADA system in the next work. While in ocean, the situation is more complex because the variability is different in upper- and deep-ocean. It needs much deeper and further work to explore the inflation in this CESM-ECDA system.

In this study, our purpose is to document the design and evaluation of the online CESM-ECDA system instead of providing a climate reanalysis product. Only several one-year perfect twin experiments and a three-year analysis experiment with real observation are conducted. In follow-up studies, we plan to complete a half century climate reanalysis within an improved CDA system using EnOI-Like filtering (Yu et al., 2019) which can effectively solve the problem of redistribution between model integration and assimilation, in which only one dynamical model member is integrated.

The online CESM-ECDA system reported in this study uses multiple ensemble members to carry out the assimilation process. The required computing resources are large for such an ensemble-based CDA system with the full complexity CGCM to execute, especially when using a high-resolution configuration (e.g., the CESM-HR, Zhang et al., 2020a). Besides, observations of other types and variables need to be further assimilated into the system. In addition, the current CESM-ECDA system is only a weakly coupled system in which the observations in one component cannot directly update the state in another component. It is worth mentioning that some ocean dynamic processes (particularly in the Tropics, such as ENSO) have influences over long spatial scale. However, depending on the reliability of statistical correlation, such as the ensemble size, the localization radius is a tunable parameter in practical data assimilation. Considering the compressibility and that the Rossby radius of deformation in atmosphere is general larger than ocean, the impact radius of atmosphere is larger than ocean in this work. We highlight here that an appropriate utilization of localization is important in the real data assimilation and coupled reanalysis, and more studies shall be further explored.

It is worth mentioning that a high-resolution configuration of CESM has been performed and evaluated thoroughly for century-long climate simulations (Small et al., 2014; Zhang et al., 2020a), and participated in the High-Resolution Model Intercomparison Project (HighResMIP, Roberts et al., 2020). A 500-year preindustrial control simulation and a 250-year

historical and future climate simulation have also been completed and evaluated (Zhang et al., 2020a; Chang et al., 2020). In this paper, the CESM-ECDA system is only evaluated with a standard resolution. In the future, the CESM-ECDA system will be assessed with the high-resolution version of CESM. Referring to the multi-timescale EnOI-like high-efficiency approximate filter (Yu et al., 2019), our ultimate goal is to develop a computationally efficient CDA system suitable for the CESM-HR (e.g., 25-km ADA system within CAM-SE and 10-km ODA system within POP2) using only one CESM integration instead of multiple ensemble members. This CDA system with CESM-HR is expected to be used to produce a high-resolution coupled reanalysis with CESM using various real observations. Therefore, many work remain to be done in the future. The ability to assimilate real observations of various types needs to be included in the future, by which similarities and differences with the previous studies (e.g., Zhang et al., 2007; Lu et al., 2020) can be compared and the important climate phenomena such as El Niño–Southern Oscillation (ENSO) and Atlantic meridional overturning circulation (AMOC) can also be further explored. In addition, the cross-domain coupled error covariance is desired to be included in the future to extend the current weakly CDA system to a strongly one.

6 Code availability

645 The codes of CESM-ECDA System are available at ZENODO via <https://doi.org/10.5281/zenodo.5733849>.

7 Data availability

The data used in this work is available at ZENODO via <https://doi.org/10.5281/zenodo.5733849>.

8 Author contributions

SZ, WZ, JS, and YJ initiated this research, proposed most ideas, and co-led paper writing.

650 SJ, YJ led the process of development & research and contributed equally to this work.

All authors contributed to the improvement of ideas, software testing, experimental evaluation, and paper writing/proofreading.

9 Competing interests

The authors declare that they have no conflict of interest.

Acknowledgments

655 The research is supported by the Chinese NFS projects 41830964,41775100, 311021009 and the Key R & D program of Ministry of Science and Technology of China (2017YFC1404100, 2017YFC1404104, 2018YFC1406202), as well as

References

660 Anderson, J. L. & Anderson, S. L. (1999). A monte carlo implementation of the nonlinear filtering problem to produce ensemble assimilations and forecasts. *Monthly Weather Review*, 127(12), 2741-2758.

Anderson, J. L. (2001). An ensemble adjustment Kalman filter for data assimilation. *Monthly Weather Review*, 129(12), 2884–2903.

Anderson, J. L. (2003). A local least squares framework for ensemble filtering. *Monthly Weather Review*, 131(4), 634–642.

665 Anderson, J. L., Wyman, B., Zhang, S., Hoar, T. (2005). Assimilation of surface pressure observations using an ensemble filter in an idealized global atmospheric prediction system. *J. Atmos. Sci.*, 62, 2925–2938.

Anderson, J. L. & Collins N. (2007). Scalable Implementations of Ensemble Filter Algorithms for Data Assimilation. *Journal of Atmospheric and Oceanic Technology*, 1452–1463, DOI: <https://doi.org/10.1175/JTECH2049.1>

670 Anderson, J., Hoar, T., Raeder, K., Liu, H., Collins, N., Torn, R., Arellano, A. (2009). The Data Assimilation Research Testbed: A community facility. *Bulletin of the American Meteorological Society*, 90, 1283—1296, doi: 10.1175/2009BAMS2618.1

Arblaster, J. M., Meehl, G. A., and Karoly, D. J. (2011). Future climate change in the Southern Hemisphere: Competing effects of ozone and greenhouse gases. *Geophysical Research Letters*, 38, L02701, doi:10.1029/2010GL045384.

Asefi-Najafabady, S., Vandekar, K., Seimon, A., Lawrence, P., Lawrence, D. (2018). Climate change, population and poverty: vulnerability and exposure to heat stress in East Africa. *Climatic Change*, doi:10.1007/s10584-018-2211-5.

675 Balmaseda, M., Anderson, D. (2009). Impact of initialization strategies and observations on seasonal forecast skill. *Geophysical Research Letters*, 36, L01701, <https://doi.org/10.1029/2008GL035561>

Bitz, C. M. (2008). Some aspects of uncertainty in predicting sea ice retreat. In *Arctic Sea Ice Decline: observations, projections, mechanisms, and implications*. AGU Geophysical Monograph Series, 180, edited by E. deWeaver, C. M. Bitz, and B. Tremblay, pp. 63–76, American Geophysical Union.

680 Bloom, S. C., Takacs, L. L., A. M. da Silva, & D Ledvina. (1996). Data assimilation using incremental analysis updates. *Monthly Weather Review*, 124(6), 1256.

Browne, P. A. & Leeuwen, P. J. van (2015). Twin experiments with the equivalent weights particle filter and HadCM3. *Q. J. R. Meteorol. Soc.* 141: 3399–3414, DOI:10.1002/qj.2621

685 Browne, P. A., Rosnay, P., Zuo H., Bennett, A. & Dawson, A. (2019). Weakly Coupled Ocean–Atmosphere Data Assimilation in the ECMWF NWP System. *Remote Sens.*, 11, 234; doi:10.3390/rs11030234

Browne, P.A. & Wilson, S. (2015). A simple method for integrating a complex model into an ensemble data assimilation system using MPI. *Environmental Modelling & Software* 68, 122–128.

Carton, J. A., Chepurin, G. A. & Chen, L. (2018). SODA3: A New Ocean Climate Reanalysis. *Journal of Climate*, 31, 6967–6983, DOI: <https://doi.org/10.1175/JCLI-D-18-0149.1>

690 Chandan, D. and Peltier, W. R. (2018). On the mechanisms of warming the mid-Pliocene and the inference of a hierarchy of climate sensitivities with relevance to the understanding of climate futures. *Climate of the Past*, 14, 825-856.

Chang, P., Zhang, S., Danabasoglu, G., Yeager, S. G., Fu, H., Wang, H., et al. (2020). An unprecedented set of high-resolution earth system simulations for understanding multiscale interactions in climate variability and change. *Journal of Advances in Modeling Earth Systems*, 12, e2020MS002298. <https://doi.org/10.1029/2020MS002298>

695 Cheng, W., Curchitser, E., Ladd, C., Stabeno, P., and Wang, M. (2014). Influences of sea ice on the Eastern Bering Sea: NCAR CESM simulations and comparison with observations. *Deep Sea Research II*, 109, 27–38, doi: 10.1016/j.dsr2.2014.03.002.

700 Chiodo, G., Garcia-Herrera, R., Calvo, N., Vaquero, J. A., Añel, and Matthes, K. (2016). The impact of a future solar minimum on climate change projections in the Northern Hemisphere. *Environmental Research Letters*, 11(3), 034015 doi:10.1088/1748-9326/11/3/034015.

705 Coelho, C. A. S., and Goddard, L. (2009). El Niño–induced tropical droughts in climate change projections. *Journal of Climate*, 22, 6456–6476, doi:10.1175/2009JCLI3185.1.

710 Collins, M., 2002: Climate predictability on interannual to decadal time scales: The initial value problem. *Climate Dyn.*, 19, 671–692

715 Compo, G.P., Whitaker, J.S., Sardeshmukh, P.D., Matsui, N., Allan, R.J., Yin, X., Gleason, B.E., Vose, R.S., Rutledge, G., Bessemoulin, P., Brönnimann, S., Brunet, M., Crouthamel, R.I., Grant, A.N., Groisman, P.Y., Jones, P.D., Kruk, M.C., Kruger, A.C., Marshall, G.J., Maugeri, M., Mok, H.Y., Nordli, Ø., Ross, T.F., Trigo, R.M., Wang, X.L., Woodruff, S.D. and Worley, S.J. (2011), The Twentieth Century Reanalysis Project. *Q.J.R. Meteorol. Soc.*, 137: 1-28. <https://doi.org/10.1002/qj.776>

Danabasoglu, G., Lamarque, J. F., Bacmeister, J., Bailey, D. A., DuVivier, A. K., Edwards, J., et al. (2020). The Community Earth System Model version 2 (CESM2). *Journal of Advances in Modeling Earth Systems*, 12(2), e2019MS001916. <https://doi.org/10.1029/2019MS001916>

720 Dee D, and Coauthors (2011) The ERA-Interim reanalysis: Configuration and performance of the data assimilation system. *Q. J. R. Meteor. Soc.*, 137, 553–597, <https://doi.org/10.1002/qj.828>.

Dennis, J. M., Edwards, J., Evans, K. J., et al. (2012). CAM-SE: A scalable spectral element dynamical core for the Community Atmosphere Model. *The International Journal of High Performance Computing Applications*, 26(1) 74–89, DOI: 10.1177/1094342011428142

725 Derber J. & Rosati A. (1989) A global oceanic data assimilation system. *Journal Phys Oceanogr* 19:1333–1347

Evans, K. J., Lauritzen, P. H., Mishra, S. K., et al. (2013). AMIP Simulation with the CAM4 Spectral Element Dynamical Core. *Journal of Climate*, 26, 689–709, DOI: 10.1175/JCLI-D-11-00448.1

730 Evensen, G. (1994). Sequential data assimilation with a nonlinear quasi-geostrophic model using Monte Carlo methods to forecast error statistics. *Journal of Geophysical Research*, 99(5), 10,143–10,162. <https://doi.org/10.1029/94JC00572>

Evensen, G. (2003). The ensemble Kalman filter: Theoretical formulation and practical implementation. *Ocean Dynamics*, 53, 343–367. <https://doi.org/10.1007/s10236-003-0036-9>

Fasullo, J. T., and Nerem, R. S. (2016). Interannual variability in global mean sea level estimated from the CESM large and last millennium ensembles. *Water*, 8 (11), 491, doi:10.3390/w8110491

735 Gantt, B., He, J., Zhang, X., Zhang, Y. and Nenes, A. (2014). Incorporation of Advanced Aerosol Activation Treatments into CESM/CAM5: Model Evaluation and Impacts on Aerosol Indirect Effects. *Atmospheric Chemistry and Physics*, 14, 7485–7497.

Gaspari, G., & Cohn, S. E. (1999). Construction of correlation functions in two and three dimensions. *Quarterly Journal of the Royal Meteorological Society*, 125(554).

Glotfelty, T., He, J., and Zhang, Y. (2017). The impact of future climate policy scenarios on air quality and aerosol/cloud interactions using an advanced version of CESM/CAM5. Part II: Future trend analysis and impacts of projected anthropogenic emissions. *Atmospheric Environment*, 152, 531-552.

Goldenson, N., Doherty, S. J., Bitz, C. M., Holland, M. M., Light, B., and Conley, A. J. (2012). Arctic climate response to forcing from light-absorbing particles in snow and sea ice in CESM. *Atmospheric Chemistry and Physics*, 12, 7903-7920, doi:10.5194/acp-12-7903-2012.

Compo G. P., Whitaker J. S., and coauthors (2011). The Twentieth Century Reanalysis Project. *Q. J. R. Meteorol. Soc.* 137: 1–28.

Goosse, H., and Holland, M. M. (2005). Mechanisms of interdecadal Arctic climate variability in the Community Climate System Model CCSM2. *Journal of Climate*, 18, 3552-3570.

740 Gropp, W., Lusk, E., Doss, N., & Skjellum, A. (1996). A high-performance, portable implementation of the mpi message passing interface standard. *Parallel Computing*, 22(6), 789-828.

Gropp, W., Lusk, E., & Thakur, R. (1999). *Using MPI-2: Advanced Features of the Message-Passing Interface*. MIT Press.

Han, G, Wu, X., Zhang, S., Liu, Z., and Li, W. (2013). Error covariance estimation for coupled data assimilation using a Lorenz atmosphere and a simple pycnocline ocean model. *Journal of Climate*, 26(24), 10218-10231.

745 Hunke, E. C., & Lipscomb, W. H. (2008). CICE: The Los Alamos sea ice model user's manual, version 4. Los Alamos National Laboratory Tech. Rep. LA-CC-06-012.

Karspeck, A.R., Yeager, S., Danabasoglu, G., Hoar, T., Collins, N., Raeder, K., Anderson, J. and Tribbia, J. (2013). An Ensemble Adjustment Kalman filter for the CCSM4 ocean component. *Journal of Climate*, 26, 7392–7413.

750 Karspeck, A. R., Danabasoglu, G., Anderson, J., Karol, S., & Craig, A. (2018). A global coupled ensemble data assimilation system using the community earth system model and the data assimilation research testbed. *Quarterly Journal of the Royal Meteorological Society*, 144(717).

Kleist, D. T., Parrish, D. F., Derber, J. C., Treadon, R., Wu, W.-S. and Lord S. (2009). Introduction of the GSI into the NCEP Global Data Assimilation System. *Monthly Weather Review*, 24, 1691–1705.

755 Laloyaux, P., Balmaseda, M., Dee, D., Mogensen, K. & Janssen P. (2016). A coupled data assimilation system for climate reanalysis. *Q. J. R. Meteorol. Soc.* 142: 65–78, DOI:10.1002/qj.2629

Lawrence, D. M., Oleson, K. W., Flanner, M. G., Thornton, P. E., Swenson, S. C., Lawrence, P. J., et al. (2011). Parameterization improvements and functional and structural advances in version 4 of the Community Land Model. *Journal of Advances in Modeling Earth Systems*, 3, MS000045, <https://doi.org/10.1029/2011MS000045>

760 Levitus, S., Antonov, J. I., Wang, J., Delworth, T. L., Dixon, K. W. and Broccoli, A. J. (2001). Anthropogenic warming of Earth's climate system. *Science*, 292(5515), 267-270.

Levitus, S., Antonov, J. I. and Boyer, T. P. (2005). Warming of the world ocean, 1955–2003. *Geophys. Res. Lett.*, 32, L02604.

Levitus, S., and Coauthors (2012). World ocean heat content and thermosteric sea level change (0–2000 m), 1955–2010. *Geophys. Res. Lett.*, 39, L10603.

765 Lu, F., Liu, Z., Zhang, S., Liu, Y. (2015). Strongly coupled data assimilation using leading averaged coupled covariance (LACC). Part II: CGCM applications. *Monthly Weather Review*, 143(11):4645–4659.

Lu, L., Zhang, S., Yeager, S. G., et al. (2020). Impact of coherent ocean stratification on AMOC reconstruction by coupled data assimilation with a biased model. *Journal of Climate*, 33, 7319-7334, <https://doi.org/10.1175/JCLI-D-19-0735.1>.

770 Mu, L., Nerger, L., Tang, Q., Loza, S. N., Sidorenko, D., Wang, Q et al. (2019). Toward a Data Assimilation System for Seamless Sea Ice Prediction Based on the AWI Climate Model. . *Journal of Advances in Modeling Earth Systems*, 12, e2019MS001937. <https://doi.org/10.1029/2019MS001937>

Neale, R. B., Gettelman, A., Park, S., Chen, C.-C., Lauritzen, P. H., Williamson, D. L., et al. (2012). Description of the NCAR Community Atmosphere Model (CAM 5.0), NCAR Tech. Note NCAR/TN-486+STR (pp. 1–289). Boulder, CO: National Center for Atmospheric Research.

775 Nerger, L., Hiller, W., Schroter, J. (2005). PDAF—the parallel data assimilation framework: experiences with Kalman filtering. In: Zwiefelhofer, W., Mozdzynski, G. (Eds.), *Use of High Performance Computing in Meteorology—Proceedings of the 11. ECMWF Workshop*. World Scientific, pp. 63–83.

Nerger, L. and Hiller, W. (2013). Software for Ensemble-based Data Assimilation Systems – Implementation Strategies and Scalability, *Comput. Geosci.*, 55, 110–118.

780 Nerger, L., Tang Q. and Mu L. (2020). Efficient ensemble data assimilation for coupled models with the Parallel Data Assimilation Framework: example of AWI-CM (AWI-CM-PDAF 1.0). *Geosci. Model Dev.*, 13, 4305–4321. <https://doi.org/10.5194/gmd-13-4305-2020>

Penny, S. G., Akella, S., Alves, O., & et al., (2017). "Coupled Data Assimilation for Integrated Earth System Analysis and Prediction: Goals, Challenges and Recommendations". WMO, WWRP 2017-3

785 Raeder, K., Anderson, J. L., Collins, N., Hoar, T. J., & Pincus, R. (2012). DART/CAM: an ensemble data assimilation system for cesm atmospheric models. *Journal of Climate*, 25(18), 6304–6317.

Rayner, N., and Coauthors (2003). Global analyses of sea surface temperature, sea ice, and night marine air temperature since the late nineteenth century. *J. Geophys. Res. Atmos.*, 108, <https://doi.org/10.1029/2002JD002670>.

790 Roberts, M. J., Jackson, L. C., Roberts, C. D., Meccia, V., Docquier, D., Koenigk, T., et al. (2020). Sensitivity of the Atlantic meridional overturning circulation to model resolution in CMIP6 HighResMIP simulations and implications for future changes. *Journal of Advances in Modeling Earth Systems*, 12, e2019MS002014. <https://doi.org/10.1029/2019MS002014>

Rosati, A., Miyakoda, K., Gudgel, R. (1997). The impact of ocean initial conditions on ENSO forecasting with a coupled model. *Monthly Weather Review*, 125, 754–772

Saha, S., Nadiga, S., Thiaw, C., Wang, J. (2006). The NCEP climate forecast system. *Journal of Climate*, 27, 2185–2208, <https://doi.org/10.1175/JCLI3812.1>

795 Saha, S., and coauthors (2010). The NCEP Climate Forecast System Reanalysis. *Bulletin of the American Meteorological Society*, 1015–1058, DOI: <https://doi.org/10.1175/2010BAMS3001.1>

Skachko, S., Buehner, M., Laroche, S., Lapalme, E., Smith, G., Roy, F., Surcel-Colan, D., Bélanger, J.-M. & Garand, L. (2019). Weakly coupled atmosphere–ocean data assimilation in the Canadian global prediction system (v1). *Geosci. Model Dev.*, 12, 5097–5112, <https://doi.org/10.5194/gmd-12-5097-2019>

800 Sluka, T. C., Penny, S. G., Kalnay, E., Miyoshi, T. (2016). Strongly coupled enkf data assimilation in coupled ocean–atmosphere models. In: The 96th AMS Annual Meeting, “Earth System Science in Service to Society,” 10–14 January 2016 in New Orleans, Louisiana

Small, R. J., Bacmeister, J., Bailey, D., Baker, A., Bishop, S., Bryan, F., et al. (2014). A new synoptic scale resolving global climate simulation using the community earth system model. *Journal of Advances in Modeling Earth Systems*, 6, 1065–1094. <https://doi.org/10.1002/2014MS000363>

805 Smith, R. D., Jones, P., Briegleb, B., Bryan, F., Danabasoglu, G., Dennis, J., et al. (2010). The parallel ocean program (POP) reference manual. Los Alamos National Laboratory tech. Rep. LAUR-10-01853.

Poli, P., and Coauthors, (2013). The data assimilation system and initial performance evaluation of the ECMWF pilot reanalysis of the 20th-century assimilating surface observations only (ERA-20C). *ECMWF ERA Rep.* 14, 59 pp.

810 Tang, Q., Mu, L., Sidorenko, D., Goessling, H., Semmler, T. & Nerger, L. (2020). Improving the ocean and atmosphere in a coupled ocean–atmosphere model by assimilating satellite sea-surface temperature and subsurface profile data. *Q. J. R. Meteorol. Soc.*, 146:4014–4029.

Tippett, M. K., Anderson, J. L., Bishop, C. H., Hamill, T. M., & Whitaker, J. S. (2003). Ensemble square root filters. *Monthly Weather Review*, 131(7), 1485–1490.

815 Whitaker, J. S., Compo, G. P., Wei, X., Hamill, T. M. (2004). Reanalysis without radiosondes using ensemble data assimilation. *Mon. Weather Rev.*, 132, 1190–1200.

Yu, X., Zhang S., Li J. et al. (2019). A multi-timescale EnOI-Like high-efficiency approximate filter for coupled model data assimilation. *Journal of Advances in Modeling Earth Systems*, 11, 45–63, <https://doi.org/10.1029/2018MS001504>.

Zhang, F. Q., Snyder, C., & Sun, J. (2004). Impacts of initial estimate and observation availability on convective-scale data assimilation with an ensemble kalman filter. *Monthly Weather Review*, 132(5), 1-16.

Zhang, S., & Anderson, J. L. (2003). Impact of spatially and temporally varying estimates of error covariance on assimilation in a simple atmospheric model. *Tellus Series A: Dynamic Meteorology and Oceanography*, 55, 126–147.

Zhang, S., Harrison M. J., Wittenberg A. T., Rosati A., Anderson J. L., Balaji V. (2005). Initialization of an ENSO forecast system using a parallelized ensemble filter. *Monthly Weather Review*, 133(11):3176–3201

Zhang, S., M. J. Harrison, A. Rosati, and A. Wittenberg (2007). System design and evaluation of coupled ensemble data assimilation for global oceanic climate studies. *Monthly Weather Review*, 135, 3541-3564, <https://doi.org/10.1175/MWR3466.1>.

Zhang, S. & Rosati, A. (2010a). An Inflated Ensemble Filter for Ocean Data Assimilation with a Biased Coupled GCM. *Monthly Weather Review*, 138(10):3905-3931, DOI: 10.1175/2010MWR3326.1

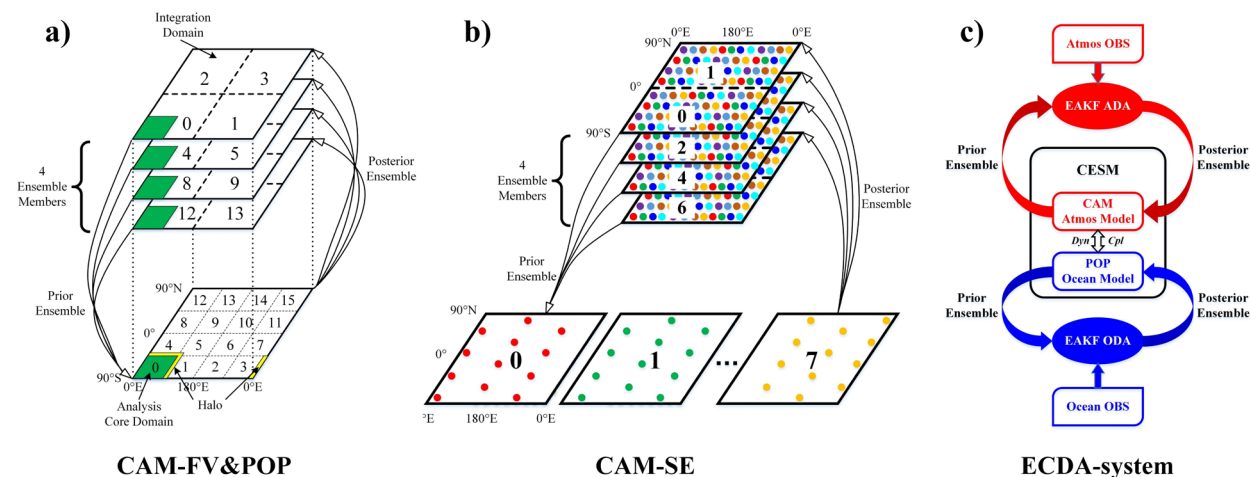
Zhang, S., Rosati, A. & Delworth T. (2010b). The Adequacy of Observing Systems in Monitoring the Atlantic Meridional Overturning Circulation and North Atlantic Climate. *Journal of Climate*, 23:5311–5324

Zhang, S. (2011). A study of impacts of coupled model initial shocks and state-parameter optimization on climate prediction using a simple pycnocline prediction model. *Journal of Climate*, 24:6210–6226

Zhang, S., Fu H., Wu L., et al. (2020a). Optimizing high-resolution Community Earth System Model on a heterogeneous many-core supercomputing platform. *Geoscientific Model Development*, 13, 4809-4829, <https://doi.org/10.5194/gmd-13-4809-2020>.

Zhang, S., Liu Z., Zhang X., et al. (2020b). Coupled data assimilation and parameter estimation in coupled ocean–atmosphere models: a review. *Climate Dynamics*, 54:5127–5144, <https://doi.org/10.1007/s00382-020-05275-6>

840 Figures:



845 **Figure 1. a)** The parallel domain decomposition and the online ensemble collection-distribution of a scalar field with CAM-FV. The four ensemble members are integrated forward in time in parallel, using four processors each member. At analysis time, the ensemble members are synchronized and the global four-element ensemble vectors are decomposed onto all 16 analysis processors. For each physical field, each analysis processor sequentially uses the observations to update the ensemble vectors at each grid point in its core domain (green) and halo (yellow). Once all nearby observations have been assimilated, the updated ensemble vectors in the core domains are transmitted back to the integration processors, completing the cycle.

850 **b)** The parallel domain decomposition and the online ensemble collection-distribution of a scalar field with CAM-SE. Different from CAM-FV, CAM-SE uses the cubed-sphere grid. To address this grid change, the implementation of domain decomposition with CAM-SE adopts a similar fashion to that used in DART (Anderson et al., 2009). This new method allows to "randomly" assign model states to different PEs. And the calculation of forward operator is realized based on the MPI2 remote memory access (RMA). At analysis time, the ensemble members are synchronized and the global ensemble vectors are randomly decomposed onto all 8 PEs (grid points with same color in the figure).

855 **c)** The parallel domain decomposition and the online ensemble collection-distribution of a scalar field with CAM-SE. Different from CAM-FV, CAM-SE uses the cubed-sphere grid. To address this grid change, the implementation of domain decomposition with CAM-SE adopts a similar fashion to that used in DART (Anderson et al., 2009). This new method allows to "randomly" assign model states to different PEs. And the calculation of forward operator is realized based on the MPI2 remote memory access (RMA). At analysis time, the ensemble members are synchronized and the global ensemble vectors are randomly decomposed onto all 8 PEs (grid points with same color in the figure).

860

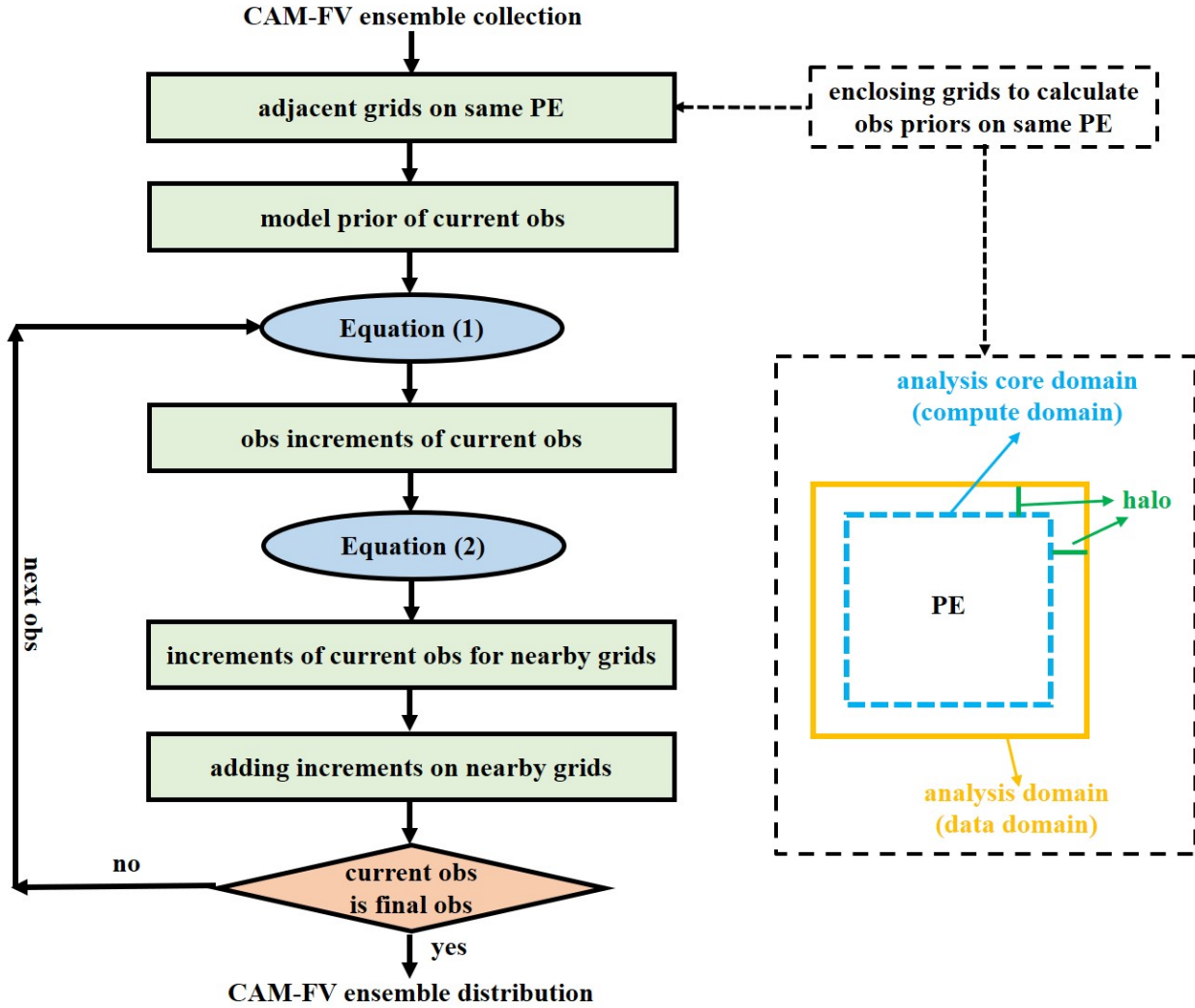
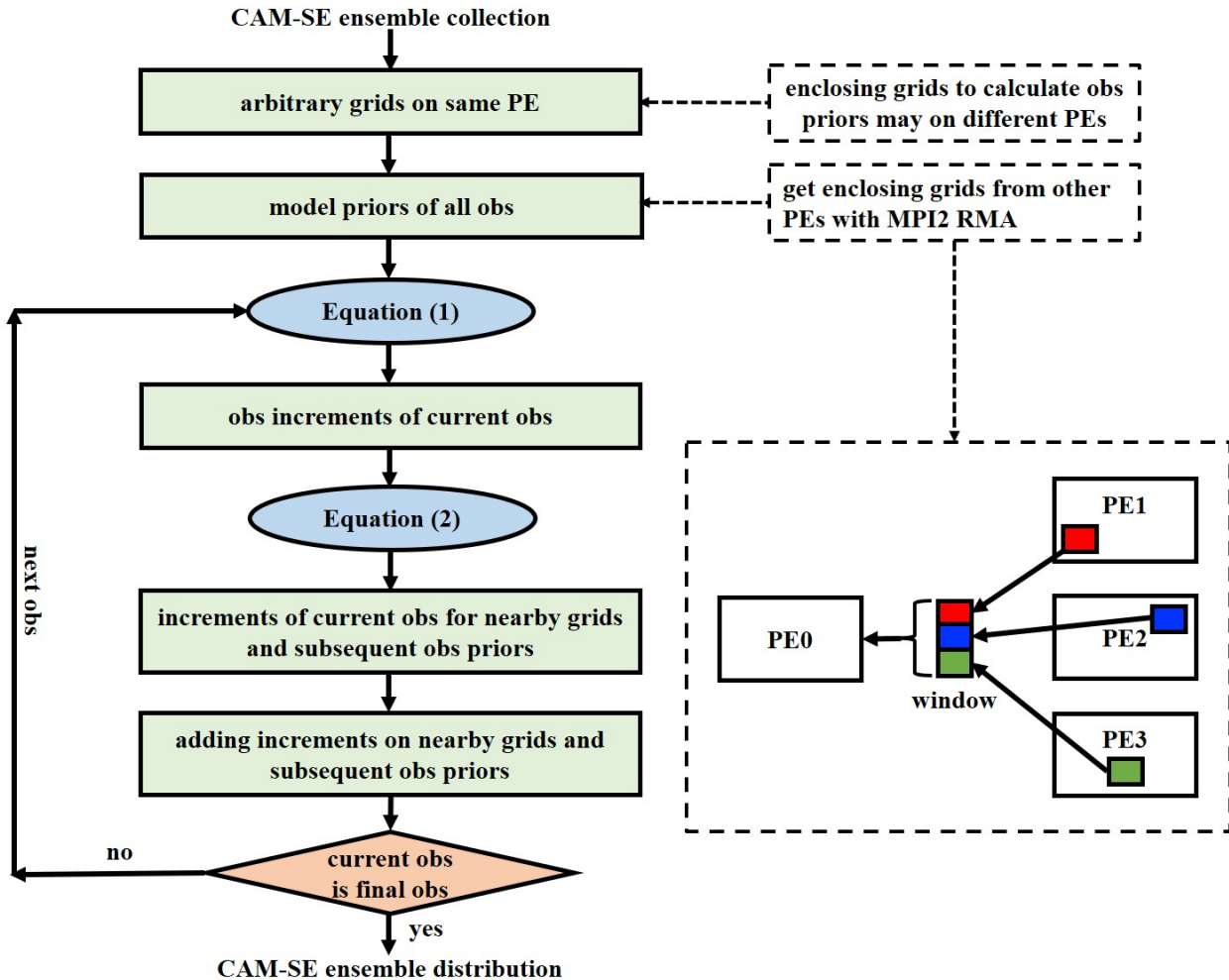


Figure 2. Schematic of the implementation of the sequential EAKF algorithm with CAM-FV. The implementation is based on the two-step method of EAKF. The decomposition strategy allows adjacent grids to be divided into the same analysis domain (i.e., onto the same analysis PE). One analysis core domain (compute domain) and its halo constitute one analysis domain (data domain). When the observations at a given time are available, only the prior ensemble of a single observation is first computed. Then each observation is assimilated sequentially according to the two-step EAKF algorithm. The observational increments of an observation only regress on the nearby model states.



870 Figure 3. Schematic of the implementation of the parallel EAKF algorithm with CAM-SE. The implementation is also based on the
 875 two-step method of EAKF. In CAM-SE, the grid points are decomposed onto the analysis PEs via an arbitrary way. Therefore, the
 computation of the forward observation operator may need to obtain values from other PEs, which is realized through the MPI2
 RMA technique. The lower-right dashed rectangular illustrates an example of grabbing data from PEs 1 – 3 to PE0 via a virtual
 window of RMA. When the observations at a given time are available, the prior ensembles for all observations are computed. The
 observational increments of an observation regress not only on the nearby model states, but also on the subsequent observation prior
 ensembles.

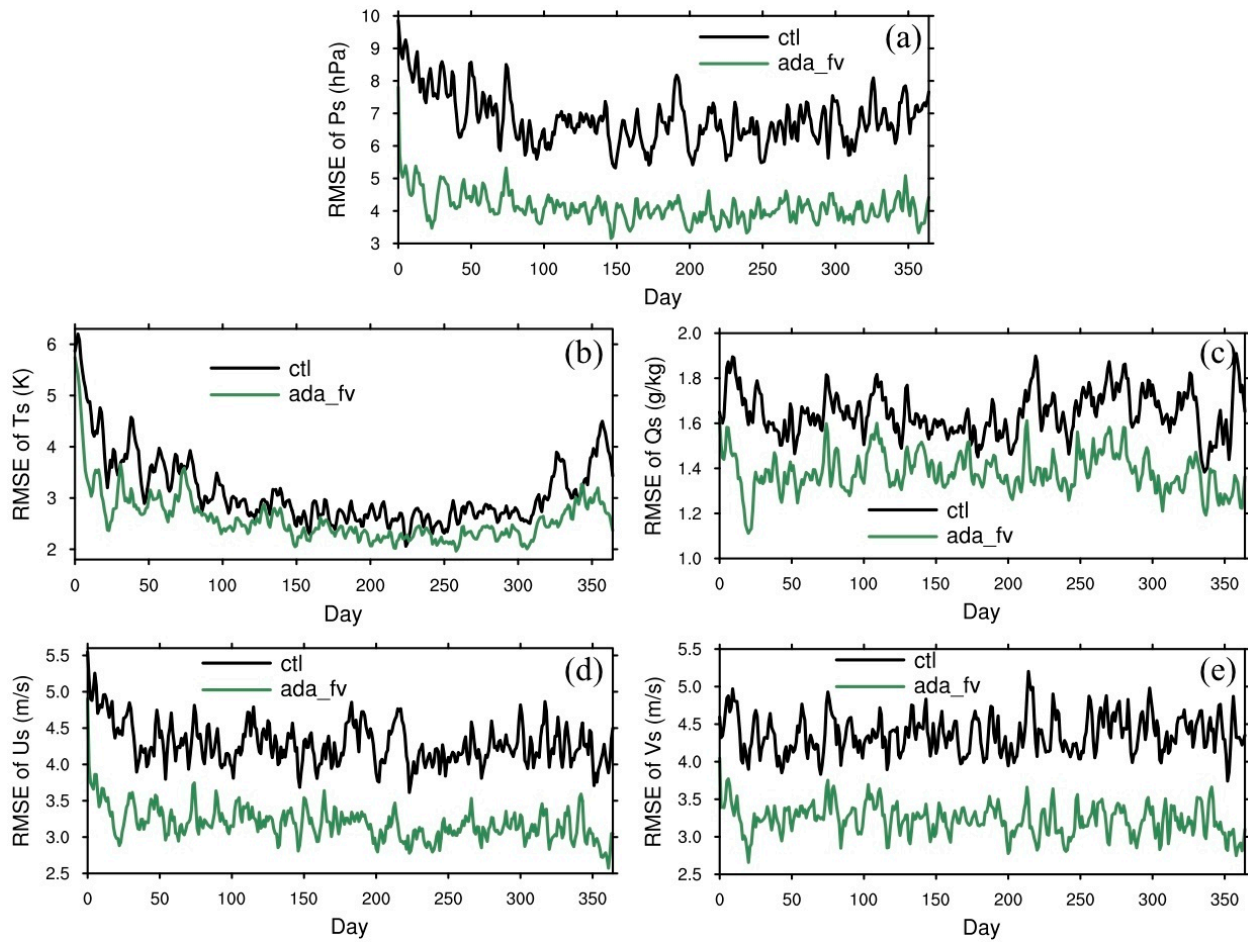


Figure 4. Time series of RMSEs of (a) surface pressure P_s , (b) surface temperature T_s , (c) surface specific humidity Q_s , (d) surface zonal wind U_s , and (e) surface meridional wind V_s from *ctl* and *ada_fv*.

880

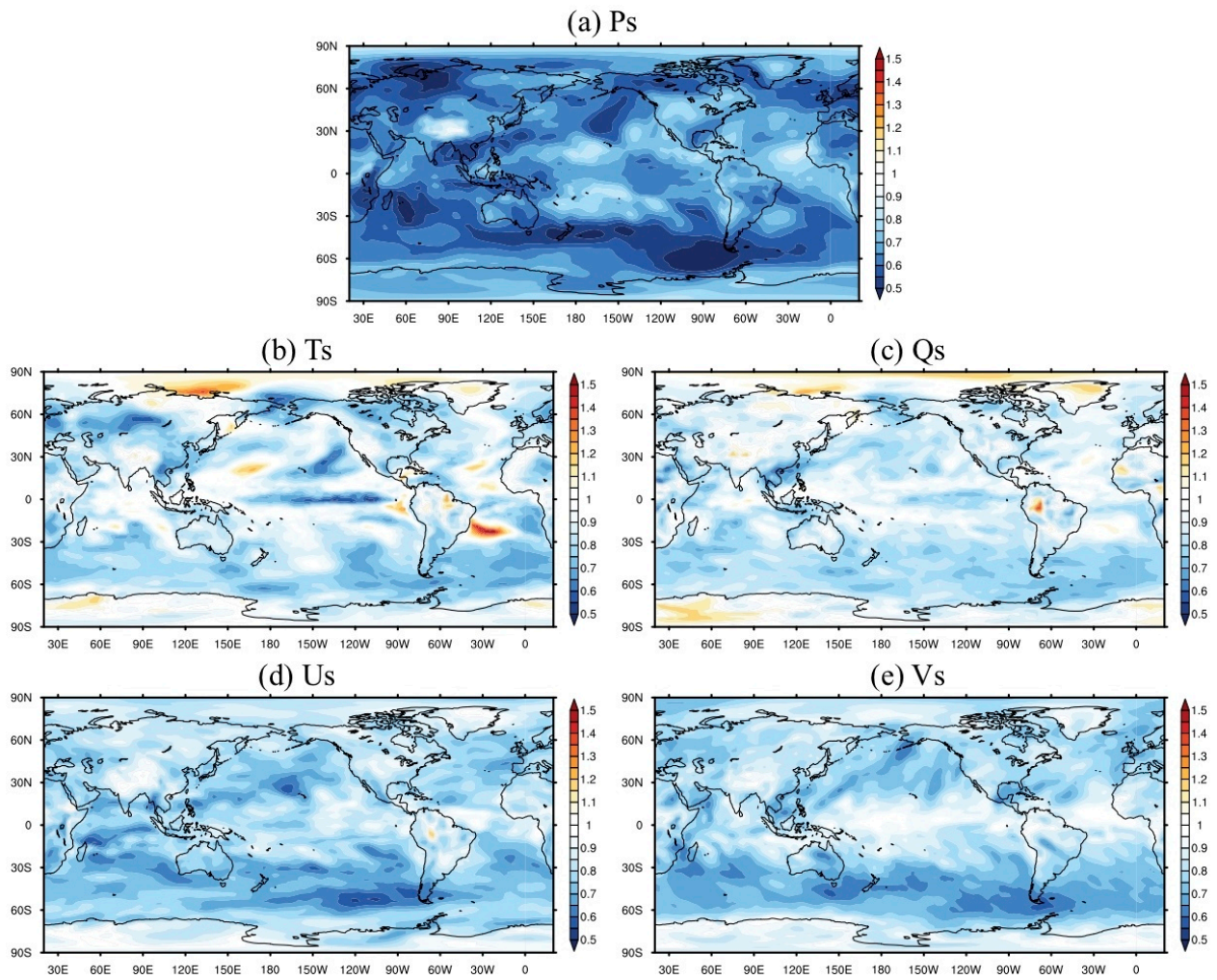


Figure 5. The distribution of the RMSE ratio (ada_fv/ctl) of (a) surface pressure Ps, (b) surface temperature Ts, (c) surface specific humidity Qs, (d) surface zonal wind Us, and (e) surface meridional wind Vs. The RMSE ratios are calculated with the data of the first month excluded.

885

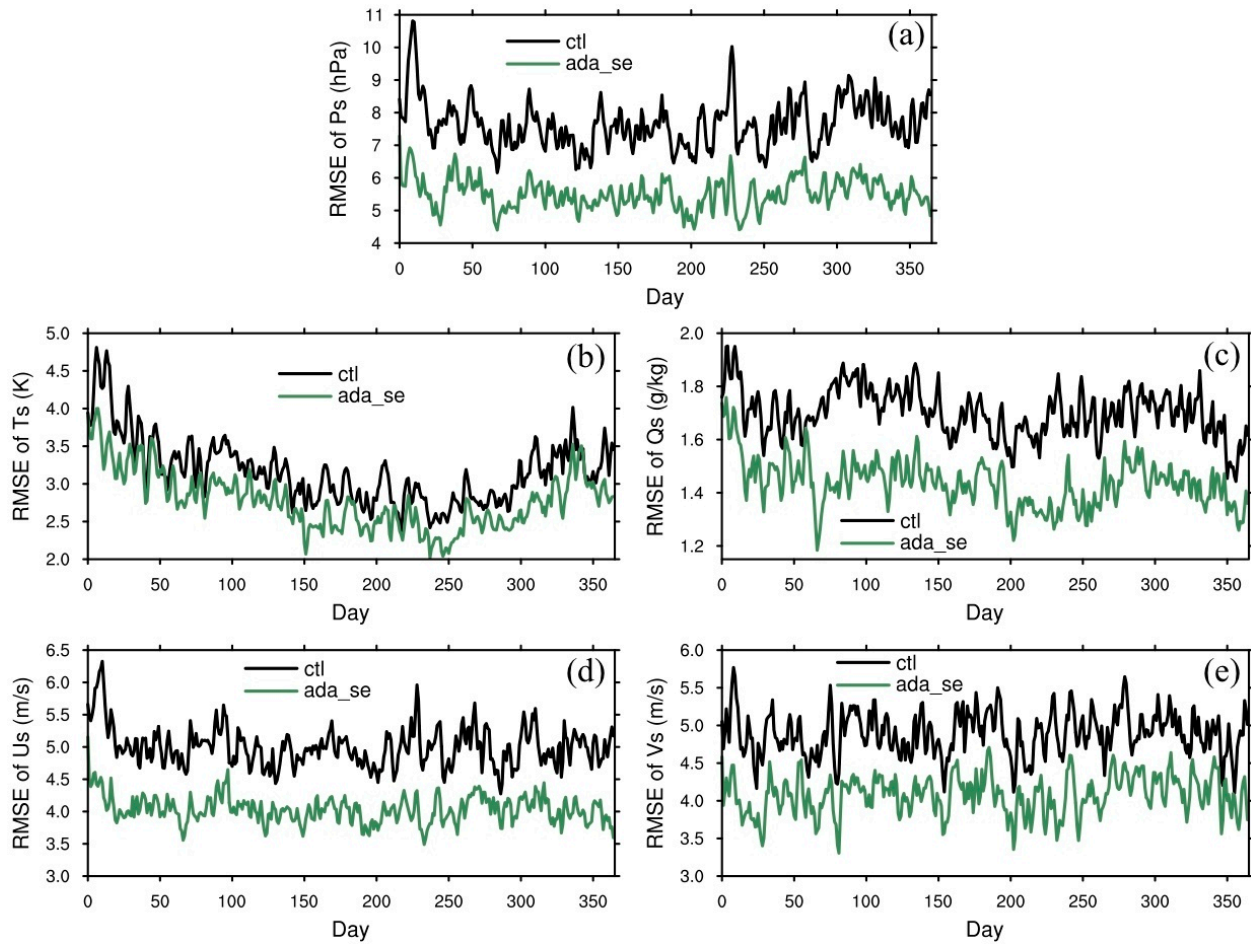


Figure 6. Time series of RMSEs of (a) surface pressure P_s , (b) surface temperature T_s , (c) surface specific humidity Q_s , (d) surface zonal wind U_s , and (e) surface meridional wind V_s from *ctl* and *ada_se*.

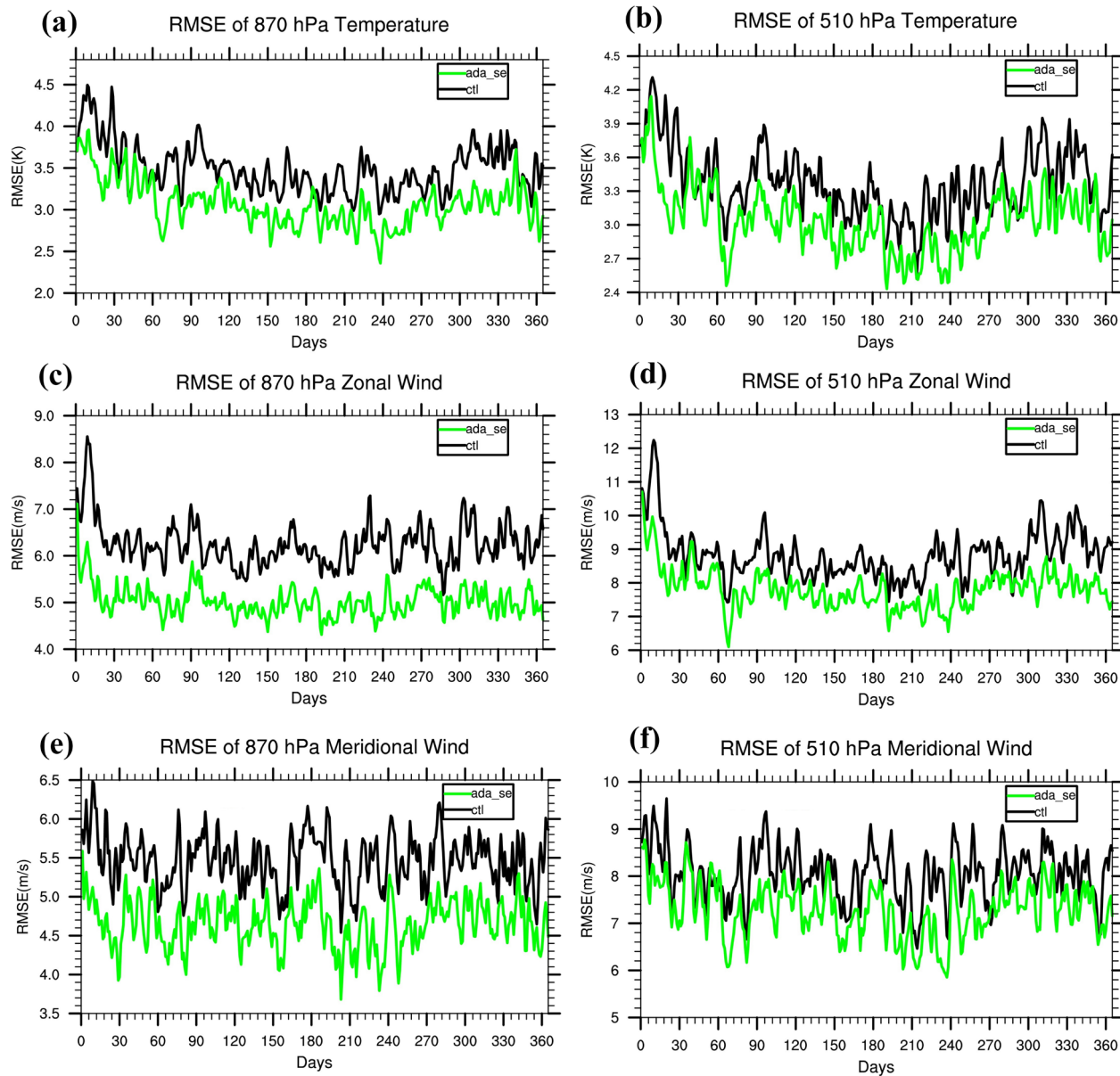
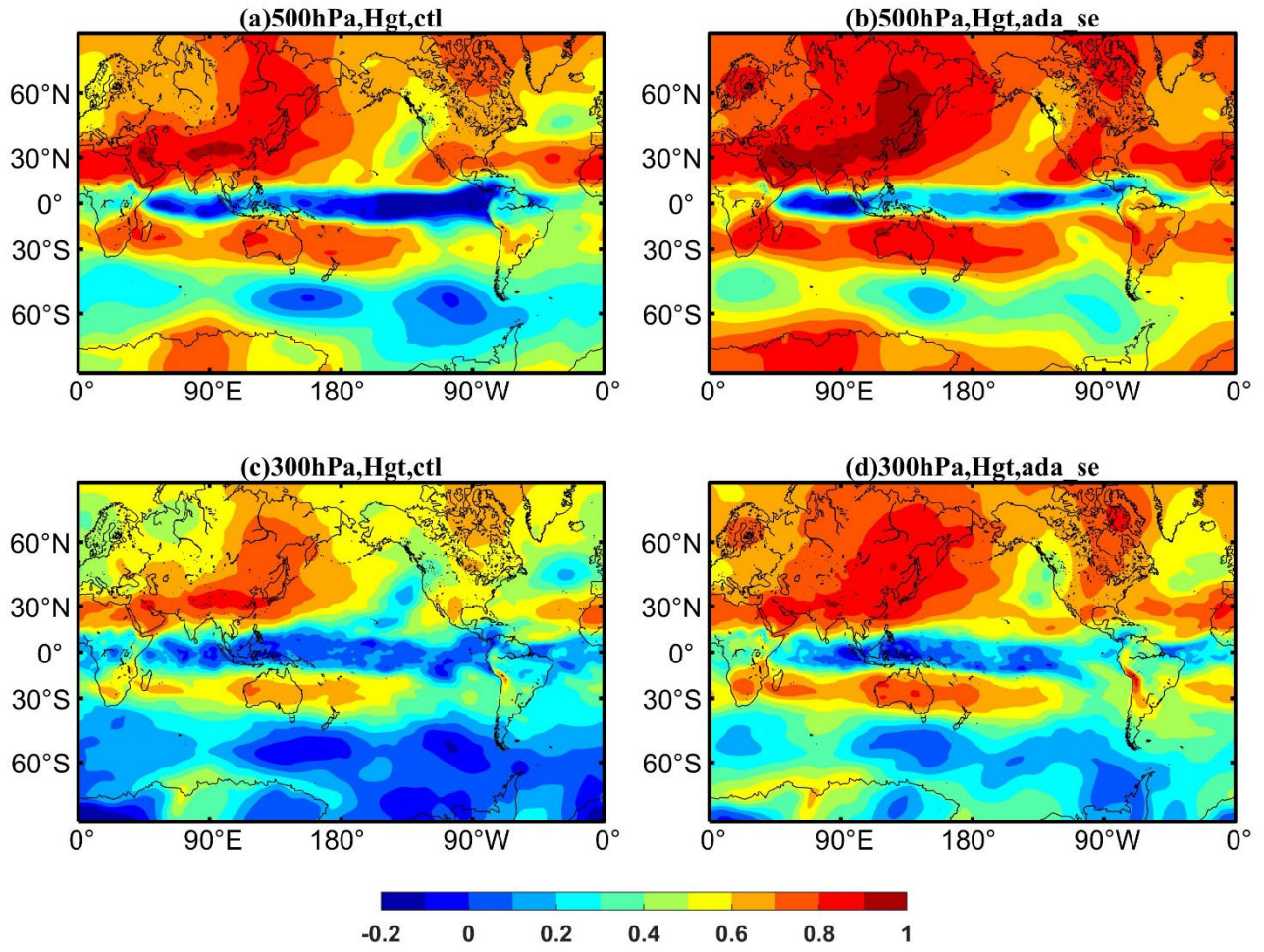
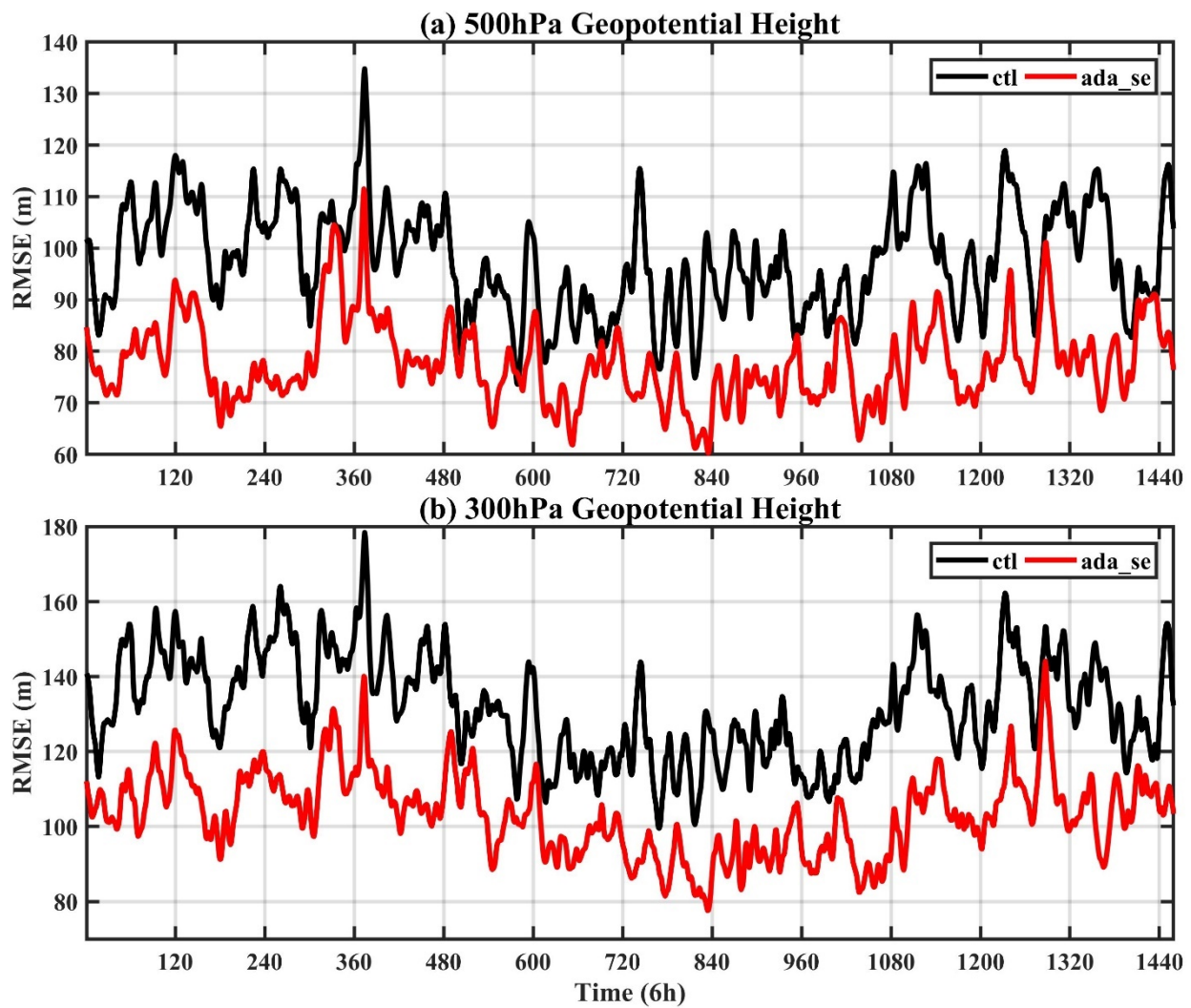


Figure 7. Time series of RMSEs of (a) 870 hPa temperature, (b) 510 hPa temperature, (c) 870 hPa zonal wind, (d) 510 hPa zonal wind, (e) 870 hPa meridional wind and (f) 510 hPa meridional wind from *ctl* (black lines) and *ada_se* (green lines).



895

Figure 8. Map of the local anomaly correlation between four-times-daily anomalies of 500-hPa (upper) and 300-hPa (below) geopotential (a, c) between *ctl* and *truth*, and (b, d) between *ada_se* and *truth*. Anomalies are computed separately for each dataset with respect to the mean annual cycle of the period shown.



900 Figure 9. Time series of RMSEs of (a) 500-hPa geopotential, (b) 300-hPa geopotential from ctl (black lines) and ada_se (red lines).

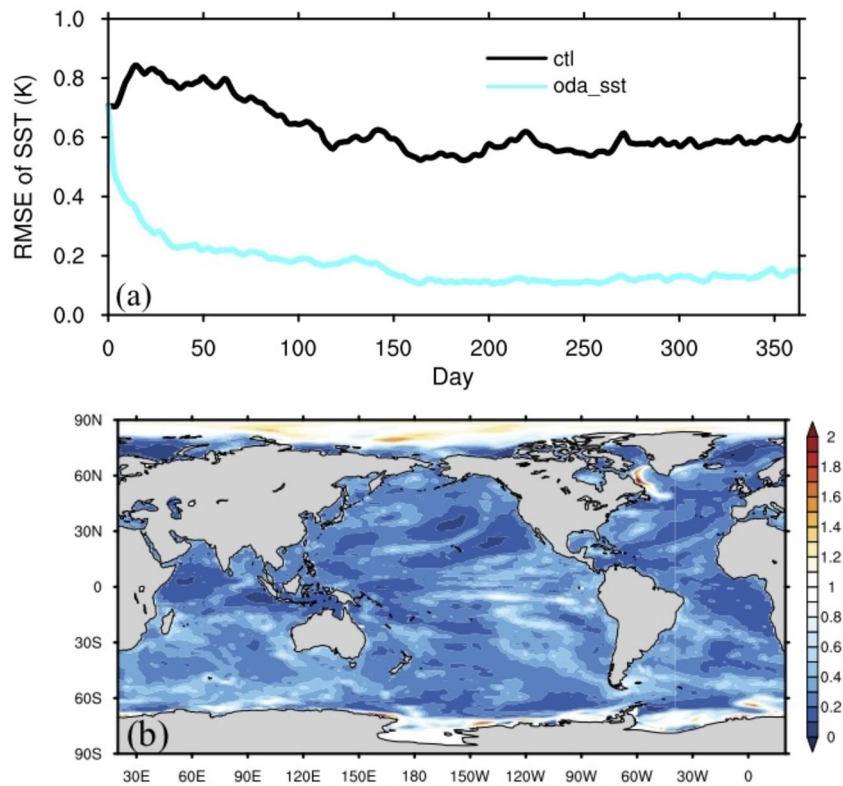
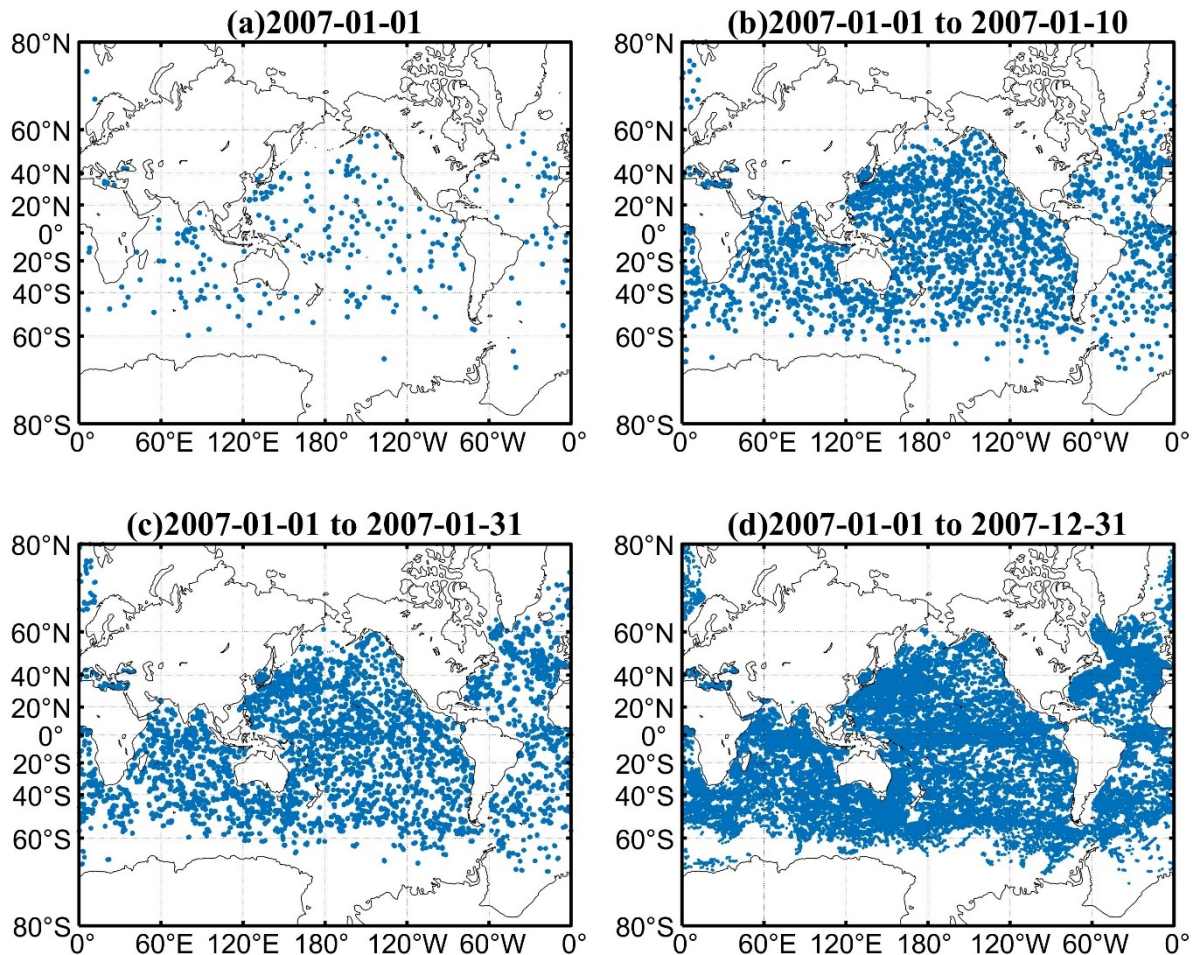


Figure 10. a) Time series of RMSE of SST from **ctl** and **oda_sst**, and b) the distribution of the RMSE ratio (**oda_sst/ctl**) of SST. The RMSE ratio is calculated with the data of the first three months excluded.



905
Figure 11. Argo locations on a) 2007-01-01, b)2007-01-01 to 2007-01-10, c) 2007-01-01 to 2007-01-31 and d) 2007-01-01 to 2007-12-31.

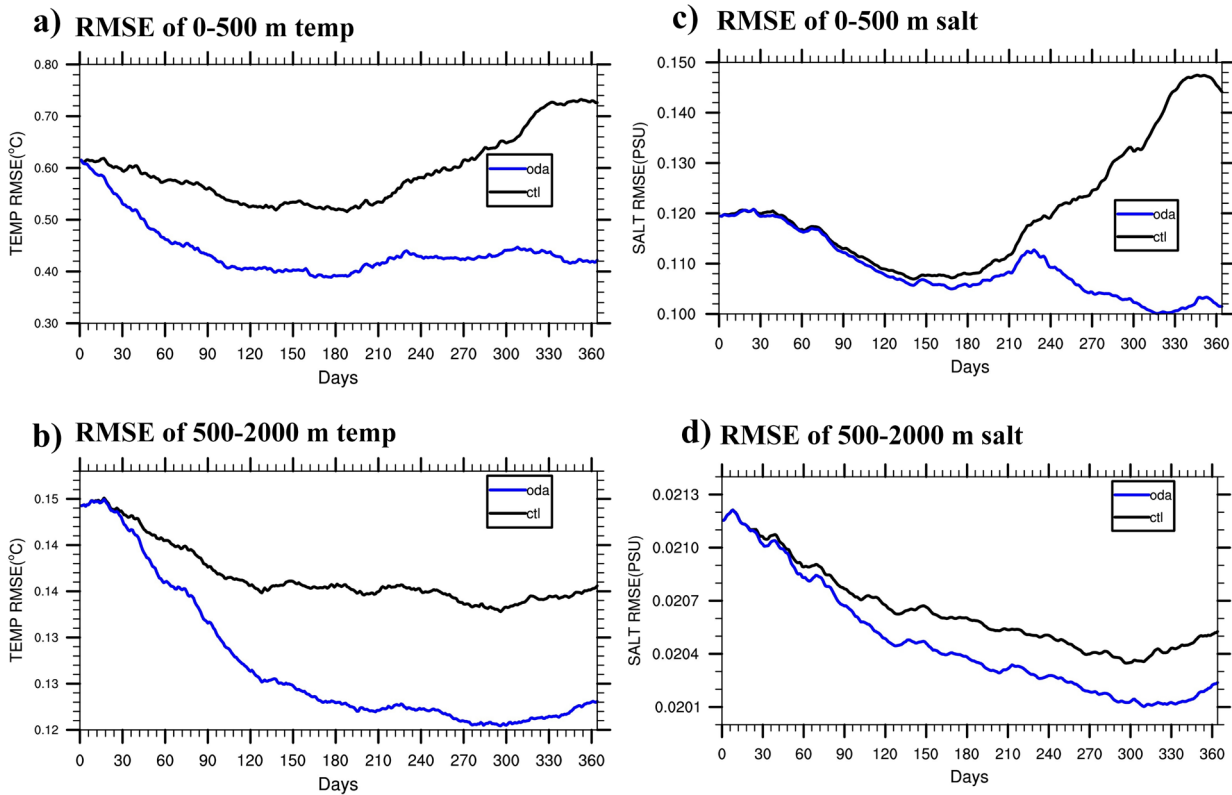


Figure 12. Time series of RMSEs of a) 0-500 m, b) 500-2000 m ocean temperature and c) 0-500 m, d) 500-2000 m ocean salinity from 910
ctl (black line) and oda (blue line).

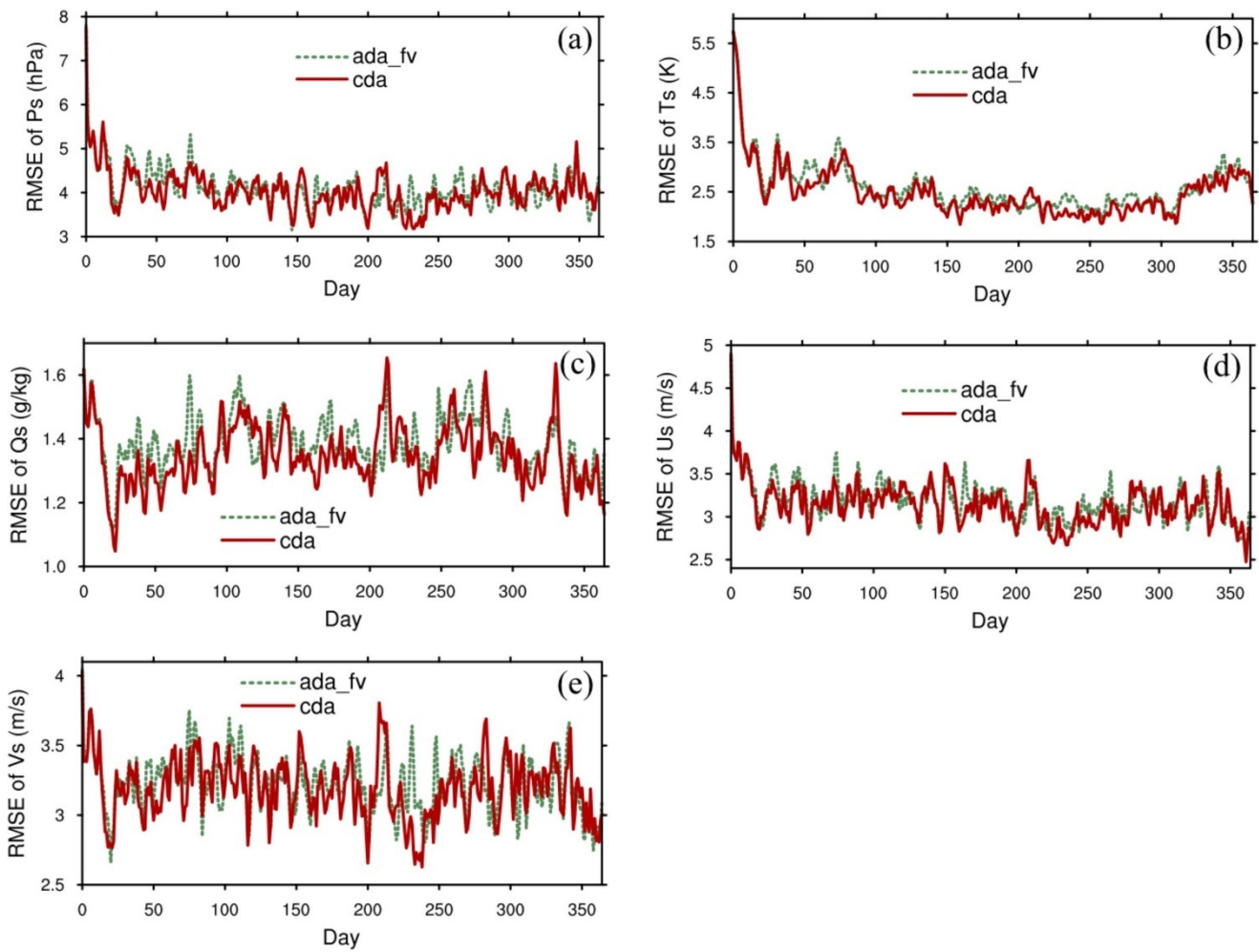


Figure 13. Time series of RMSEs of (a) surface pressure P_s , (b) surface temperature T_s , (c) surface specific humidity Q_s , (d) surface zonal wind U_s , and (e) surface meridional wind V_s from `ada_fv` and `cda`.

915

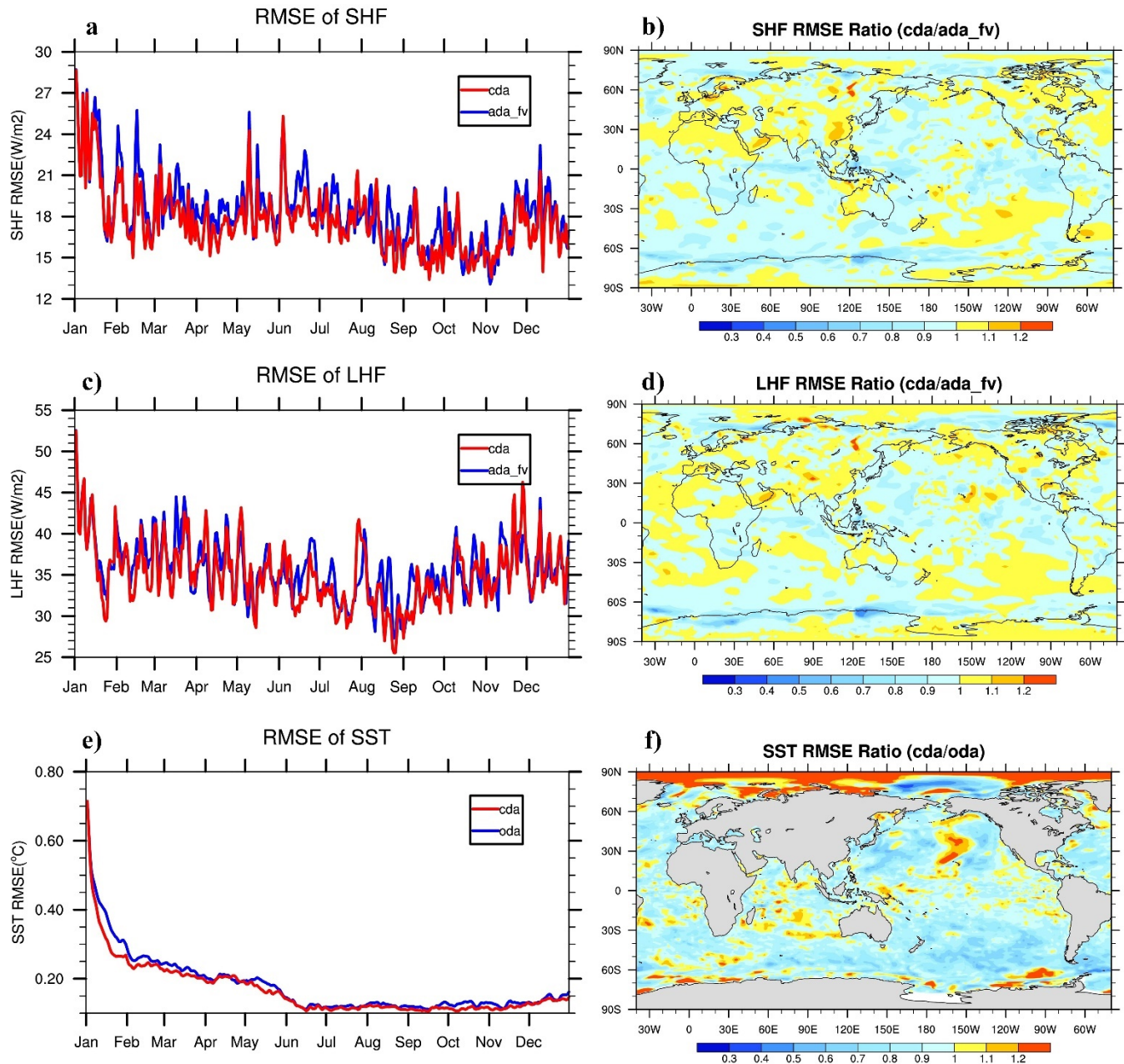


Figure 14. Time series of RMSEs of (a) sensible heat flux (SHF), (c) latent heat flux (LHF) from ada_fv and cda, (e) SST from oda_sst and cda; distribution of the RMSE ratio of (b) SHF (cda/ada_fv), (d) LHF (cda/ada_fv), and SST(cda/oda) . The RMSE ratios are calculated with the data of the first month excluded.

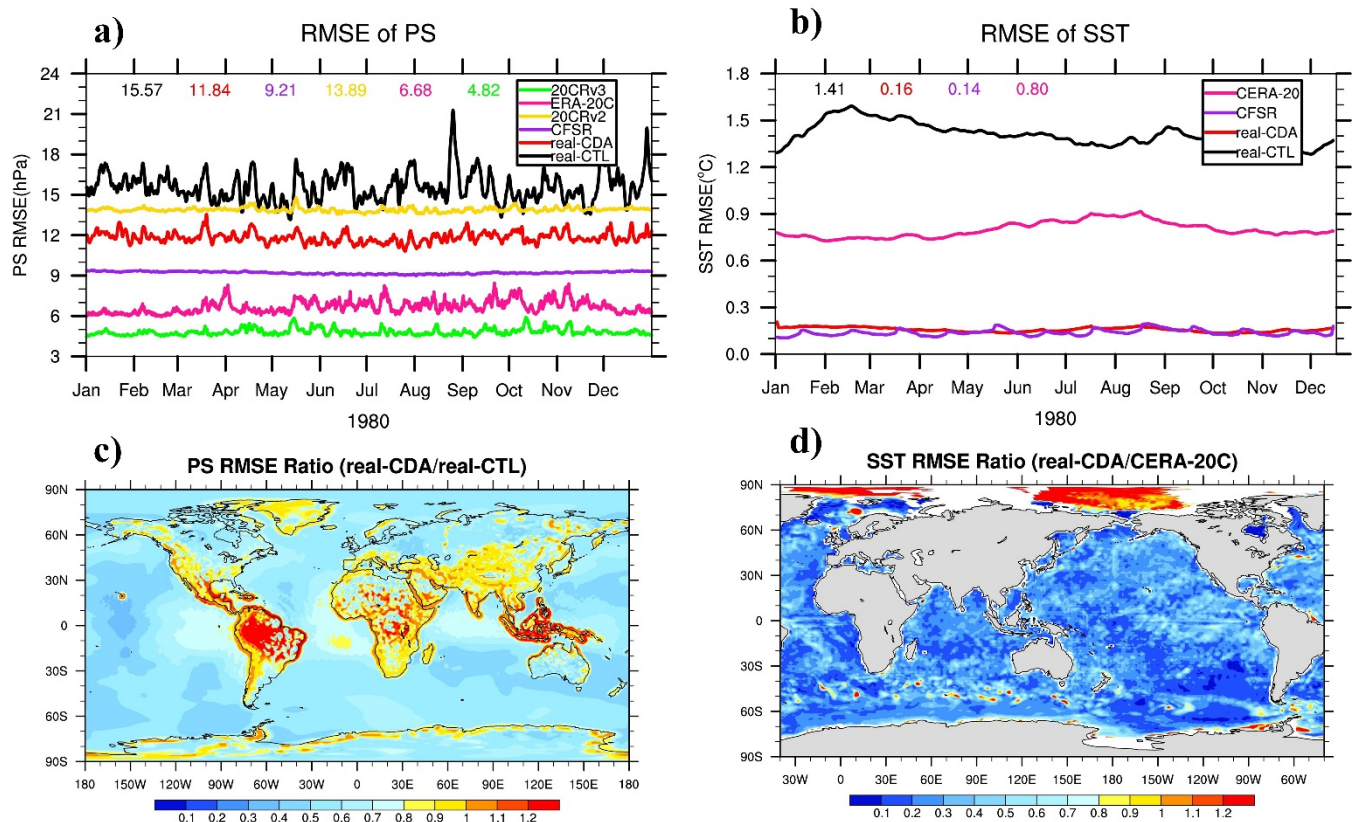


Figure 15. Time series of RMSE of a) Ps and b) SST from the real observation assimilating experiment and RMSE ratio distributions of Ps (real-CDA/real-CTL) and SST (real-CDA/CERA-20C) in 1980. The number in a) and b) are RMSEs of the mean value corresponding to each product.

925

Tables:

Table 1. List of experiments.

Experiment	DA	OBS
ctl	none	None
ada_fv	CAM-FV ADA	Ps
ada_se	CAM-SE ADA	Ps
oda_sst	POP ODA	SST
oda	POP ODA	SST + TS profile
cda	CAM-FV ADA + POP ODA	Ps + SST

Table 2. Globally averaged RMSEs of surface pressure Ps, surface temperature Ts, surface specific humidity Qs, surface zonal wind Us, and surface meridional wind Vs from ctl and ada_fv. The RMSEs are calculated with the data of the first month excluded.

930

Experiment	Ps (hPa)	Ts (K)	Qs (g/kg)	Us (m/s)	Vs (m/s)
ctl	6.68	2.99	1.64	4.24	4.36
ada_fv	4.05	2.51	1.39	3.16	3.22
reduction(%)	39.4	16.1	15.5	25.5	26.1

Table 3. Globally averaged RMSEs of surface pressure Ps, surface temperature Ts, surface specific humidity Qs, surface zonal wind Us, and surface meridional wind Vs from ctl and ada_se. The RMSEs are calculated with the data of the first month excluded.

Experiment	Ps (hPa)	Ts (K)	Qs (g/kg)	Us (m/s)	Vs (m/s)
ctl	6.17	2.47	1.58	4.62	4.49
ada_se	4.36	2.10	1.32	3.69	3.72
reduction(%)	29.4	14.9	16.2	20.1	17.0

935 **Table 4. Globally averaged RMSEs of ocean temperature and salinity vertically averaged between surface and 500 m and between 500 m and 2000 m from ctl and oda with the data of the last six months.**

Experiment	0-500m	500-2000m	0-500m	500-2000m
	T (K)	T (K)	S (PSU)	S (PSU)
ctl	0.59	0.14	0.121	0.0204
oda	0.44	0.13	0.109	0.0202
reduction(%)	25.0	7.1	9.9	1.2

Table 5. Globally averaged RMSEs of surface pressure Ps, surface temperature Ts, surface specific humidity Qs, surface zonal wind Us, surface meridional wind Vs, sensible heat flux SHF, and latent heat flux LHF from ada_fv and cda. The RMSEs are calculated with the data of the first month excluded.

Experiment	Ps (hPa)	Ts (K)	Qs (g/kg)	Us (m/s)	Vs (m/s)	SHF (W/m ²)	LHF (W/m ²)
ada_fv	4.05	2.51	1.39	3.16	3.22	17.53	40.44
cda	3.98	2.40	1.35	3.12	3.19	16.86	39.60
reduction(%)	1.8	4.3	2.4	1.3	1.1	3.8	2.1

945

Table 6. Comparison of CPU time in offline cda experiments and online cda experiments.

experiment	Run days	1 d	5 d	30 d	365 d
offline	Init Time	29m 01s	2h 25m 09s	14h 30m 55s	176h 36m 17s
	Run Time	7m 28s	37m 22s	3h 44m 16s	45h 28m 44s
	Total Time	36m 29s	3h 02m 31s	18h 15m 11s	222h 15m 01s
online	Init Time	7m 15s	7m 15s	7m 15s	7m 15s
	Run Time	7m 28s	37m 22s	3h 44m 16s	45h 28m 44s
	Total Time	14m 43s	44m 37s	3h 51m 31s	45h 35m 59s
Ratio (online/offline)	Total Time	40.35%	24.45%	21.14%	20.53%

Init Time = initialization period + input period

Run Time = model period + analysis period + output period